

VILENS: Visual, Inertial, Lidar, and Leg Odometry for All-Terrain Legged Robots

David Wisth, *Student Member, IEEE*, Marco Camurri, *Member, IEEE*, and Maurice Fallon, *Member, IEEE*
Oxford Robotics Institute, University of Oxford, Oxford, UK

Abstract—We present VILENS (Visual Inertial Lidar Legged Navigation System), an odometry system for legged robots based on factor graphs. The key novelty is the tight fusion of four different sensor modalities to achieve reliable operation when the individual sensors would otherwise produce degenerate estimation. To minimize leg odometry drift, we extend the robot’s state with a linear velocity bias term which is estimated online. This bias is only observable because of the tight fusion of this preintegrated velocity factor with vision, lidar, and IMU factors. Extensive experimental validation on the ANYmal quadruped robots is presented, for a total duration of 2 h and 1.8 km traveled. The experiments involved dynamic locomotion over loose rocks, slopes, and mud; these included perceptual challenges, such as dark and dusty underground caverns or open, feature-deprived areas, as well as mobility challenges such as slipping and terrain deformation. We show an average improvement of 62 % translational and 51 % rotational errors compared to a state-of-the-art loosely coupled approach. To demonstrate its robustness, VILENS was also integrated with a perceptive controller and a local path planner.

Index Terms—Legged robots, sensor fusion, localization, field robots.

I. INTRODUCTION

THE increased maturity of quadruped robotics has been demonstrated in initial industrial deployments, as well as impressive results achieved by academic research. State estimation plays a key role in field deployment of legged machines: without an accurate estimate of its location and velocity, the robot cannot build up a useful representation of its environment or plan and execute trajectories to reach planned goal positions.

Most legged robots are equipped with a high frequency (>250 Hz) proprioceptive state estimator for control and local mapping purposes. These are typically implemented as nonlinear filters fusing high frequency signals such as kinematics and IMU [1]. In ideal conditions (i.e., high friction, rigid terrain, slow speeds), these estimators have a limited (yet unavoidable) drift that is acceptable for local mapping and control.

However, deformable terrain, leg flexibility and foot slippage can degrade estimation performance up to the point where local terrain reconstruction is unusable and multi-step trajectories cannot be executed, even over short ranges. This problem is more evident when a robot is moving dynamically, which can be the limiting factor when crossing rough terrain.

Recent works have attempted to improve kinematic-inertial estimation accuracy by detecting unstable contacts and reducing their influence on the overall estimation [2], [3].

Manuscript received June X, 2021; revised XXXX X, 2021. Corresponding author: D. Wisth (email: davidw@robots.ox.ac.uk).

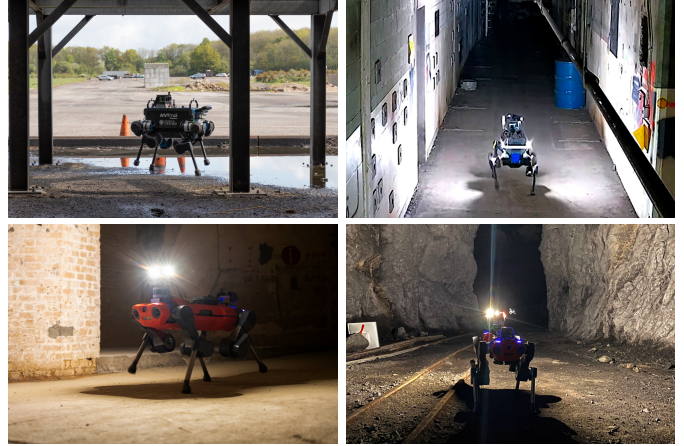


Fig. 1. VILENS has been tested on a variety of platforms. *Top-Left*: ANYmal B300 at the Fire Service College in Moreton-On-Marsh (UK). *Top-Right*: ANYmal B300 modified for the DARPA SubT Challenge (Urban Circuit) in Olympia (Washington, USA). *Bottom-Left*: ANYmal C100 in a limescale mine in Wiltshire (UK). *Bottom-Right*: ANYmal C100 in an abandoned mine in Seemühle (Switzerland). Video: <https://youtu.be/2318fiEB2cQ>

Alternatively, other approaches have incorporated additional exteroceptive sensing into the estimator to help reduce the pose error. These included either tightly coupled methods fusing camera, IMU, and kinematics [4] or loosely coupled methods combining lidar in addition to the other sensors [5], [6]. Furthermore, these approaches model the contact locations as being fixed and affected only by Gaussian noise. Both assumptions are broken when there is nonrigid terrain, kinematic chain flexibility, or foot slippage.

In our work we aim to fuse all four sensor modalities in a tightly coupled fashion, with particular focus on the proper integration of leg kinematics, even when slippage or terrain deformation occurs.

A. Motivation

Our work is motivated by the challenges and limitations of state estimation for the deployment of legged robots in extreme environments, as illustrated in Fig. 1. The DARPA SubT Challenge involves the deployment of a team of autonomous robots navigating unknown, dark, and unstructured underground environments. In such scenarios, individual sensor modalities can fail (e.g., due to camera blackouts or degenerate geometries for lidar), so robust sensor fusion is paramount. Additional requirements include limited computational budget and the need for high frequency output to update the local footstep

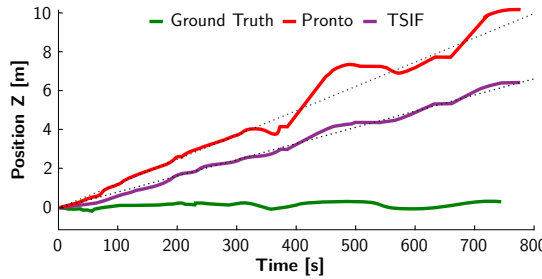


Fig. 2. Comparison between estimated robot elevation by Pronto [2] (red) and TSIF [11] (purple) kinematic-inertial state estimators, against ground truth (green) on the SMR experiment (see Section VI-B). Despite local fluctuations, the drift has a characteristic linear growth.

planner. For these reasons, we aim to use all of the sensors available on the robot (IMU, kinematics, lidar, and camera) to form constraints for lightweight sliding window optimization, as it can be more accurate than filter-based approaches [7].

When both lidar and camera fail at the same time, IMU integration alone would rapidly lead to divergence. Leg kinematics can prevent this, but special care has to be taken to fuse it with the other sensors in an effective way, especially in presence of foot impacts and terrain deformation. Fig. 2 shows this effect on the ANYmal B300 robot traveling over different terrains. Two different kinematic-inertial estimators suffer from continuous elevation drift which is approximately linear. Fahmi *et al.* [8] demonstrated that this drift can be caused by nonrigid, and nonstatic interaction of the legs and terrain during contact events.

One approach would be to further model the dynamic properties of the robot, such as torque-dependent bending [9], into the kinematic estimate or to model the terrain directly within the estimator. However, this would be robot specific and terrain dependent — improving performance in one situation but degrading it elsewhere.

Inspired by the IMU bias estimation and preintegration methods from [10], we instead propose to extend the state with a velocity bias term to estimate and reject these effects. This bias is observable when doing tight fusion with exteroceptive sensors. This novel leg odometry factor computes a velocity measurement from kinematic sensing, preintegrates it, and estimates its bias to compensate for the characteristic drift of the leg odometry on slippery or deformable ground.

B. Contributions

This paper makes the following contributions, significantly extending our previous work [12]:

- A novel factor based on joint kinematic measurements which, in contrast to [12], is fully integrated into the cost function, rather than being received from an external filter. A full derivation of the noise propagation from the joint states is also provided in the Appendix.
- Support and testing on a wider range of sensor modalities, including fisheye cameras and lidar odometry. To the best of our knowledge, this is the first smoothing algorithm to combine inertial, legged, visual and lidar data into a single factor graph. The wide support of complementary

sensor modalities is the key to operation in adverse operational conditions, such as the DARPA SubT Challenge.

- Extensive evaluation in a broad set of scenarios including different models of the ANYmal quadruped. We tested the algorithm online and integrated with both a dynamic perceptive controller [13] and an autonomous exploration planner [14].

The remainder of this article is presented as follows: in Section II we review the literature on legged state estimation with a focus on sensor fusion via smoothing methods and contact modeling; Section III formally defines the problem addressed by the paper and provides the required mathematical background; Section IV describes the factors used in our proposed graph formulation; Section V presents the implementation details of our system; Section VI presents the experimental results and an interpretation of them; Section VII concludes with final remarks.

II. RELATED WORK

We define multi-sensor state estimation as the joint processing of multiple proprioceptive and/or exteroceptive sensors to estimate the pose and velocity of a mobile robot [15]. Multi-sensor estimation can be divided into two broad categories: *filtering* and *smoothing*. Filtering methods iteratively estimate the current state from the previously estimated state and the current sensor data. All the states before the current one are marginalized out. Instead, smoothing methods jointly optimize all or part of the past states and measurements to estimate a history of robot states. In Section II-A we describe *smoothing* methods applied to multi-sensor estimation on legged robots. In Section II-B we review the relevant methods for modeling nonlinearities at the contact point during leg odometry.

A. Multi-Sensor Smoothing on Legged Robots

Multi-sensor smoothing typically involves the fusion of IMU, leg odometry, and visual tracking within a probabilistic graphical models framework, such as factor graphs. Hartley *et al.* [16] proposed the first method to incorporate leg odometry into a factor graph. They extended the floating base state with the feet contact locations and defined two new factors to incorporate forward kinematics, where a zero velocity constraint on the contact points of a foot were imposed. The two new factors were then combined with the preintegrated IMU factor from [10] and relative pose measurements from the SVO visual odometry system [17]. In [4], the same authors extended this work to support multiple footsteps in the same kinematics factor. Both works were demonstrated on the Cassie bipedal robot in controlled environments in experiments lasting <2 min.

Fourmy *et al.* [18] proposed a factor-graph based state estimation system for the Solo12 quadruped robot [19]. It fused both kinematic and dynamic information to estimate the base frame of the robot and performed online calibration of the offset between the base frame and center of mass. The authors claimed this was important for control since the center of mass of their robot was not known precisely from the CAD model. However, only very limited experimental results

were presented, where only the robot's torso moved while the feet were stationary. In the related field of motion planning, Xie *et al.* [20] modeled both the kinematics and dynamics of a 3 DoF manipulator using factor graphs. This approach took into account dynamics, contact forces, and joint actuation limits.

In our prior work [21], we proposed a tightly coupled visual-inertial-legged system based on the iSAM2 solver [22] running on the ANYmal robot. The method tracked visual features from a RealSense D435i stereo camera and optimized them as the landmarks in a factor graph. Leg odometry was only loosely coupled with relative pose factors formed using the internal state estimator running on the robot [11]. The method was demonstrated using extensive outdoor experiments in urban and industrial scenarios.

All these works were based on the assumption of a stationary point of foot contact. This assumption is violated every time there are slippages or deformations of the leg and/or the ground. Contact detection methods can help to reject sporadic slippage or deformation events. However, when these occur regularly, they need to be modeled.

B. Modeling Contact Deformation and Slippage

In legged robotics, slippage and/or deformation have typically been addressed by assuming the contact location of a stance foot is entirely static throughout the stance period (yet affected by Gaussian noise). Thus, the main focus has been on detecting and ignoring the feet that are not in fixed contact with the ground. This is a relatively simple task when a foot is equipped with force/torque sensors. In this case, a high vertical component of the measured force would imply that the contact force is within the friction cone and therefore nonslipping. However, residual errors due to model uncertainty or deformation might persist. Fahmi *et al.* [8] have shown that incorrect contact detections on soft ground (i.e., detecting a “rigid” contact while the leg and ground are still deforming) are a key contributor to leg odometry drift.

Bloesch *et al.* [1] proposed an Unscented Kalman Filter design that fused IMU and differential kinematics. The approach used a threshold on the Mahalanobis distance of the filter innovation to infer velocity measurement outliers (caused by misclassified contact legs) which were then ignored.

For systems without feet sensors, more sophisticated methods were proposed. Hwangbo *et al.* [23] presented a probabilistic approach where information from kinematics, differential kinematics and dynamics were fused together within a Hidden Markov Model (HMM). This approach was later integrated with a dynamic trotting controller and demonstrated on the ANYmal robot walking on ice [3].

Instead of a HMM, Bledt *et al.* [24] proposed to fuse information from kinematics and dynamics, as well as additional input from the controller's gait cycle within a Kalman filter. Their work was demonstrated on the Cheetah 3 robot walking on rubble.

Camurri *et al.* [2] proposed a contact detector that learned the optimal force threshold to detect a foot in contact for a specific gait, and an impact detector that adapted the measurement covariance online to reject unreliable measurements. In

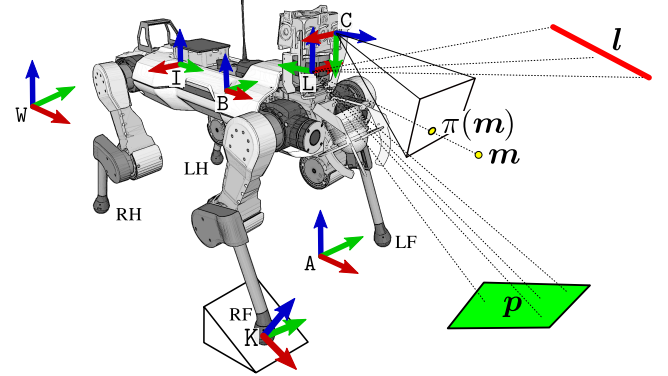


Fig. 3. Reference frames and landmark conventions. The world frame W is fixed to earth. The base frame B , the camera's optical frame C , the lidar frame L , and the IMU frame I are all rigidly attached to the robot's chassis. The feet are conventionally named: Left Front (LF), Right Front (RF), Left Hind (LH) and Right Hind (RH). When a foot touches the ground (e.g., RF), a contact frame K (perpendicular to the ground and parallel to W 's y -axis) is defined. The primitives tracked by the system are points m , lines l , and planes p . To improve numerical stability, when a new plane feature is detected, an additional local fixed anchor frame A is defined.

our previous work [12], we used this approach to fuse each leg's contribution into a single velocity measurement for our proposed factor graph method. The contact nonlinearities were modeled as a bias term on the linear velocity measurements from leg odometry. This could reduce the inconsistency between leg and visual odometry and provide a more robust pose and velocity estimate. However, the system was still dependent on an external filter to access the velocity estimates from the kinematics. Furthermore no lidar information was integrated into the system — which is now a common sensor on quadruped robots. In contrast to [12], in this work we compute the velocity measurements from kinematics internally, instead of receiving them from an external filter. This avoids the potential double usage of the IMU signal (from the filter and from the preintegrated IMU factor) and allows us to properly model the error propagation from the joints to the end effector.

III. PROBLEM STATEMENT

Our objective is to estimate the history of poses and velocities of a legged robot equipped with a combination of sensors, including: cameras (mono or stereo), IMUs, lidars, and joint sensors (encoders and torque sensors).

A. Notation

Scalars are lowercase italics (a, b, c, \dots), matrices are uppercase Roman bold ($\mathbf{A}, \mathbf{B}, \mathbf{C}, \dots$), and vectors are lowercase Roman bold ($\mathbf{a}, \mathbf{b}, \mathbf{c}, \dots$). Reference frames are indicated in typeface (A, B, C, \dots) and for physical quantities we follow the frame decorator rules from [25]. States and landmarks are bold italics ($\mathbf{a}, \mathbf{b}, \mathbf{c}, \dots$), while sensor measurements are uppercase calligraphics ($\mathcal{A}, \mathcal{B}, \mathcal{C}, \dots$). Finally, the set of time indices for a measurement are uppercase sans (A, B, C, \dots). Where appropriate, a time-dependent quantity will be shortened as $a(t_i) = a_i$.

B. Frame Definitions

The relevant reference frames are specified in Fig. 3 and include: the fixed-world frame W , the base frame B , the IMU frame I , the camera frame C (left camera, when stereo), and the lidar frame L . When a foot is in contact with the ground, a contact frame K , fixed to earth, is defined. Finally, a local anchor frame A , also fixed to earth, is defined for lidar feature tracking, as detailed in Section IV-E.

C. State Definition

The robot state at time t_i is defined as follows:

$$\mathbf{x}_i \triangleq [\mathbf{R}_i, \mathbf{p}_i, \mathbf{v}_i, \mathbf{b}_i^g, \mathbf{b}_i^a, \mathbf{b}_i^\omega, \mathbf{b}_i^v] \in \text{SO}(3) \times \mathbb{R}^{15} \quad (1)$$

where: $\mathbf{R}_i \in \text{SO}(3)$ is the orientation; $\mathbf{p}_i \in \mathbb{R}^3$ is the position; $\mathbf{v}_i \in \mathbb{R}^3$ is the linear velocity; $\mathbf{b}_i^g \in \mathbb{R}^3$ and $\mathbf{b}_i^a \in \mathbb{R}^3$ are the usual IMU gyroscope and accelerometer biases. We expand the state with angular and linear velocity biases $\mathbf{b}_i^\omega, \mathbf{b}_i^v \in \mathbb{R}^3$ to model slippage, deformations and other kinematics inaccuracies at the contact point.

Unless otherwise specified, the position ${}_W\mathbf{p}_{WB}$ and orientation \mathbf{R}_{WB} of the base are expressed in world coordinates, velocities of the base ${}_B\mathbf{v}_{WB}, {}_B\omega_{WB}$ are in base coordinates, IMU biases ${}_I\mathbf{b}^g, {}_I\mathbf{b}^a$ are expressed in the IMU frame, and the velocity biases are expressed in the base frame, ${}_B\mathbf{b}_{WB}^\omega, {}_B\mathbf{b}_{WB}^v$.

In addition to the robot state, we also estimate the position of visual and lidar landmarks. Visual landmarks \mathbf{m} are parametrized as 3D points in Euclidean space and projected onto the image plane via the function $\pi(\cdot)$ (yellow dots in Fig. 3). Lidar landmarks are parametrized as planar and linear geometric primitives (green plane \mathbf{p} and red line \mathbf{l} in Fig. 3), as detailed in [26]. For brevity, we will later refer to any of the above landmarks with \mathbf{f} .

We define the history of states and landmarks, visible up to the current time t_k , as:

$$\mathcal{X}_k \triangleq \{\mathbf{x}_i, \mathbf{m}_\ell, \mathbf{p}_\ell, \mathbf{l}_\ell\}_{i \in \mathcal{K}_k, \ell \in \mathcal{F}_k} \quad (2)$$

where \mathcal{K}_k and \mathcal{F}_k are the sets of all keyframe and landmark indices, respectively.

D. Measurements Definition

We denote with \mathcal{I}_{ij} the IMU measurements received between two consecutive keyframes i and j . Each measurement includes the proper acceleration $\tilde{\mathbf{a}}$ and the rotational velocity $\tilde{\omega}$, both expressed in the IMU frame. Similarly, we define the kinematics measurements \mathcal{K}_{ij} . These include the joint positions $\tilde{\alpha}$ and velocities $\tilde{\dot{\alpha}}$. The (mono or stereo) camera images and lidar point clouds collected at time t_i are expressed with \mathcal{C}_i and \mathcal{L}_i , respectively. In practice, camera and lidar measurements are received at different times and frequencies, so they are first synchronized before being integrated into the graph (see Section V-A).

The full set of measurements within the smoothing window is defined as:

$$\mathcal{Z}_k \triangleq \{\mathcal{I}_{ij}, \mathcal{K}_{ij}, \mathcal{C}_i, \mathcal{L}_i\}_{i, j \in \mathcal{K}_k} \quad (3)$$

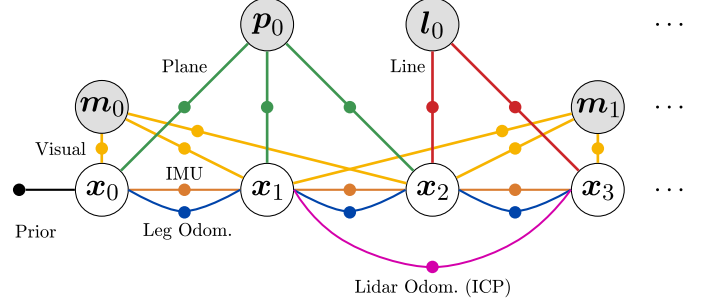


Fig. 4. VILENS factor graph structure. The factors are: prior (black), visual (yellow), lidar planes (green), lidar lines (red), preintegrated IMU (orange), preintegrated velocity (from leg odometry, blue), and lidar odometry (from ICP registration, magenta). State nodes are white, while landmarks are grey.

E. Maximum-A-Posteriori Estimation

We wish to maximize the likelihood of the measurements \mathcal{Z}_k given the history of states and landmarks \mathcal{X}_k :

$$\mathcal{X}_k^* = \arg \max_{\mathcal{X}_k} p(\mathcal{X}_k | \mathcal{Z}_k) \propto p(\mathcal{X}_0) p(\mathcal{Z}_k | \mathcal{X}_k) \quad (4)$$

Given that the measurements are assumed to be conditionally independent and corrupted by white Gaussian noise, Eq. (4) can be formulated as a least squares minimization problem of the following form:

$$\mathcal{X}_k^* = \arg \min_{\mathcal{X}_k} \|\mathbf{r}_0\|_{\Sigma_0}^2 + \sum_{i \in \mathcal{K}_k} \left(\|\mathbf{r}_{\mathcal{I}_{ij}}\|_{\Sigma_{\mathcal{I}_{ij}}}^2 + \|\mathbf{r}_{\mathcal{K}_{ij}}\|_{\Sigma_{\mathcal{K}_{ij}}}^2 + \|\mathbf{r}_{\mathbf{b}_{ij}}\|_{\Sigma_{\mathbf{b}_{ij}}}^2 + \|\mathbf{r}_{\mathcal{L}_i}\|_{\Sigma_{\mathcal{L}_i}}^2 + \sum_{\ell \in \mathcal{F}_i} \|\mathbf{r}_{\mathbf{x}_i, \mathbf{f}_\ell}\|_{\Sigma_{\mathbf{x}_i, \mathbf{f}_\ell}}^2 \right) \quad (5)$$

where each term is the squared residual error associated to a factor type, weighted by the inverse of its covariance matrix. All the residuals (except the state prior \mathbf{r}_0) are added whenever a new keyframe i is created. These include: preintegrated IMU $\mathbf{r}_{\mathcal{I}_{ij}}$ and kinematic velocity $\mathbf{r}_{\mathcal{K}_{ij}}$; IMU and kinematic velocity biases $\mathbf{r}_{\mathbf{b}_{ij}}$; lidar odometry $\mathbf{r}_{\mathcal{L}_i}$; landmarks primitives $\mathbf{r}_{\mathbf{x}_i, \mathbf{f}_\ell}$. The latter are further divided into point, line, and plane residuals:

$$\sum_{\ell \in \mathcal{F}_i} \|\mathbf{r}_{\mathbf{x}_i, \mathbf{f}_\ell}\|_{\Sigma_{\mathbf{x}_i, \mathbf{f}_\ell}}^2 = \sum_{\ell \in \mathcal{M}_i} \|\mathbf{r}_{\mathbf{x}_i, \mathbf{m}_\ell}\|_{\Sigma_{\mathbf{x}_i, \mathbf{m}_\ell}}^2 + \sum_{\ell \in \mathcal{L}_i} \|\mathbf{r}_{\mathbf{x}_i, \mathbf{l}_\ell}\|_{\Sigma_{\mathbf{x}_i, \mathbf{l}_\ell}}^2 + \sum_{\ell \in \mathcal{P}_i} \|\mathbf{r}_{\mathbf{x}_i, \mathbf{p}_\ell}\|_{\Sigma_{\mathbf{x}_i, \mathbf{p}_\ell}}^2 \quad (6)$$

IV. FACTOR GRAPH FORMULATION

In this section, we describe the measurements, residuals and covariances of the factors which form the graph shown in Fig. 4. For convenience, we summarize the IMU factors from [10] in Section IV-A; our novel velocity factor is detailed in Section IV-B; Sections IV-C and IV-D describe the bias and stereo visual residuals, which are adapted from [10], [12] to include the velocity bias term and support for fisheye cameras, respectively. We also briefly introduce the lidar factor residuals from [26] in Section IV-E. Finally, the lidar odometry residual is detailed in Section IV-F.

A. Preintegrated IMU Factors

As in [10], the IMU measurements are preintegrated to constrain the pose and velocity between two consecutive nodes of the graph, and provide high frequency state updates between them. This uses a residual of the form:

$$\mathbf{r}_{\mathcal{I}_{ij}} = \left[\mathbf{r}_{\Delta \mathbf{R}_{ij}}^T, \mathbf{r}_{\Delta \mathbf{v}_{ij}}^T, \mathbf{r}_{\Delta \mathbf{p}_{ij}}^T \right]^T \quad (7)$$

where the individual elements of the residual are defined as:

$$\mathbf{r}_{\Delta \mathbf{R}_{ij}} = \text{Log} \left(\Delta \tilde{\mathbf{R}}_{ij}(\mathbf{b}_i^g) \right) \mathbf{R}_i^T \mathbf{R}_j \quad (8)$$

$$\mathbf{r}_{\Delta \mathbf{v}_{ij}} = \mathbf{R}_i^T (\mathbf{v}_j - \mathbf{v}_i - \mathbf{g} \Delta t_{ij}) - \Delta \tilde{\mathbf{v}}_{ij}(\mathbf{b}_i^g, \mathbf{b}_i^a) \quad (9)$$

$$\begin{aligned} \mathbf{r}_{\Delta \mathbf{p}_{ij}} = \mathbf{R}_i^T & \left(\mathbf{p}_j - \mathbf{p}_i - \mathbf{v}_i \Delta t_{ij} - \frac{1}{2} \mathbf{g} \Delta t_{ij}^2 \right) \\ & - \Delta \tilde{\mathbf{p}}_{ij}(\mathbf{b}_i^g, \mathbf{b}_i^a) \end{aligned} \quad (10)$$

As explained in more detail in [10], this formulation does not require recomputation of the integration between the two keyframes connected by the factor every time the linearization point changes. This makes the fusion of the high frequency signal from the IMU and lower frequency measurements from camera and lidar computationally feasible.

The Eqs. (8)–(10) depend on the optimized states and preintegrated measurements $\Delta \tilde{\mathbf{R}}_{ij}$, $\Delta \tilde{\mathbf{v}}_{ij}$, $\Delta \tilde{\mathbf{p}}_{ij}$. For convenience, we report them here (for the incorporation of the bias update and other details, see [10]):

$$\Delta \tilde{\mathbf{R}}_{ij} = \prod_{k=i}^{j-1} \text{Exp} ((\tilde{\omega}_k - \mathbf{b}_i^g) \Delta t) \quad (11)$$

$$\Delta \tilde{\mathbf{v}}_{ij} = \sum_{k=i}^{j-1} \Delta \tilde{\mathbf{R}}_{ik} (\tilde{\mathbf{a}}_k - \mathbf{b}_i^a) \Delta t \quad (12)$$

$$\Delta \tilde{\mathbf{p}}_{ij} = \sum_{k=i}^{j-1} \left[\Delta \tilde{\mathbf{v}}_{ik} \Delta t + \frac{1}{2} \Delta \tilde{\mathbf{R}}_{ik} (\tilde{\mathbf{a}}_k - \mathbf{b}_i^a) \Delta t^2 \right] \quad (13)$$

These are associated to the corresponding preintegrated noises, which can be expressed in iterative form:

$$\begin{bmatrix} \delta \phi_{i,k+1} \\ \delta \mathbf{v}_{i,k+1} \\ \delta \mathbf{p}_{i,k+1} \end{bmatrix} = \begin{bmatrix} \Delta \tilde{\mathbf{R}}_{k,k+1}^T & \mathbf{0} & \mathbf{0} \\ -\Delta \tilde{\mathbf{R}}_{ik} (\tilde{\mathbf{a}}_k - \mathbf{b}_i^a) \wedge \Delta t & \mathbf{I} & \mathbf{0} \\ -\frac{1}{2} \Delta \tilde{\mathbf{R}}_{ik} (\tilde{\mathbf{a}}_k - \mathbf{b}_i^a) \wedge \Delta t^2 & \mathbf{I} \Delta t & \mathbf{I} \end{bmatrix} \begin{bmatrix} \delta \phi_{i,k} \\ \delta \mathbf{v}_{i,k} \\ \delta \mathbf{p}_{i,k} \end{bmatrix} + \begin{bmatrix} \mathbf{J}_R^k \Delta t & \mathbf{0} \\ \mathbf{0} & \Delta \tilde{\mathbf{R}}_{ik} \Delta t \\ \mathbf{0} & \frac{1}{2} \Delta \tilde{\mathbf{R}}_{ik} \Delta t^2 \end{bmatrix} \begin{bmatrix} \boldsymbol{\eta}^g \\ \boldsymbol{\eta}^a \end{bmatrix} \quad (14)$$

from which the covariance $\Sigma_{\mathcal{I}_{ij}}$ can be computed.

B. Preintegrated Leg Odometry Factors

Inspired by the preintegrated IMU factor, we define here the preintegrated velocity factor from leg odometry. The factor is used to estimate the position of the robot from high frequency joint kinematics measurements.

To derive a velocity signal from leg kinematics, we first need to estimate the stance legs, i.e., the set of legs in stable contact with the ground (Section IV-B1). Then, we fuse the odometry from these legs as a combined velocity measurement (Section IV-B2). To model the nonlinearities at the contact point, the linear velocity bias and its residuals are introduced

in Section IV-B3. Finally, the preintegrated measurements and their residuals are described in Sections IV-B4 and IV-B5, respectively.

1) *Stance Estimation*: The feet of the robot are approximated as points. For simplicity, the contact point is assumed to be on a fixed point at the center of the foot of the robot, which in our case is a soft rubber sphere with a 2 cm radius. Since no direct force measurement is assumed to be available, we compute the Ground Reaction Force (GRF) at each foot from the dynamics equation of motion:

$$\mathbf{f} = - (\mathbf{J}_p(\boldsymbol{\alpha})^T)^\dagger \left(\boldsymbol{\tau} + \mathbf{h}(\boldsymbol{\alpha}) + \mathbf{F}^T \begin{bmatrix} \dot{\boldsymbol{\omega}} \\ \dot{\mathbf{v}} \end{bmatrix} \right) \quad (15)$$

where † indicates the Moore-Penrose pseudo inverse operation, $\boldsymbol{\alpha}$ are the joint positions, $\mathbf{J}_p(\cdot) \in \mathbb{R}^{3 \times 3}$ is the Jacobian of the forward kinematics function relative to the point foot (later indicated with $\mathbf{f}_p(\cdot) \in \mathbb{R}^3$), $\boldsymbol{\tau}$ are the joint torques, $\mathbf{h}(\boldsymbol{\alpha})$ are the Coriolis terms, and \mathbf{F} is the matrix of spatial forces required at the floating base to support unit accelerations about each joint variable [27].

For each leg that is in contact with the ground, we assume *rigid, nonslipping contact*. By thresholding the vertical component of the GRF for each foot, we get the set of binary contact states for all the legs. We indicate the subset of the legs in contact as $S \subseteq L$, with $L = \{\text{LF}, \text{RF}, \text{LH}, \text{RH}\}$ (Fig. 3).

2) *Combined Kinematic Velocity Measurement*: Given a leg $s \in S$, we can compute the linear velocity of the robot's floating base at time t_i as follows:

$$\mathbf{v}_s = -\mathbf{J}_p(\boldsymbol{\alpha}) \dot{\boldsymbol{\alpha}} - \boldsymbol{\omega} \times \mathbf{f}_p(\boldsymbol{\alpha}) \quad (16)$$

Both the joint positions and velocities are measured from encoders and corrupted by additive zero-mean Gaussian noise:

$$\tilde{\boldsymbol{\alpha}} = \boldsymbol{\alpha} + \boldsymbol{\eta}^\alpha \quad (17)$$

$$\tilde{\dot{\boldsymbol{\alpha}}} = \dot{\boldsymbol{\alpha}} + \boldsymbol{\eta}^{\dot{\alpha}} \quad (18)$$

where $\boldsymbol{\eta}^\alpha, \boldsymbol{\eta}^{\dot{\alpha}}$ are available from the sensor specifications. After substituting (17) and (18) into Eq. (16), we can formulate a linear velocity measurement [1]:

$$\mathbf{v}_s = -\mathbf{J}_p(\tilde{\boldsymbol{\alpha}} - \boldsymbol{\eta}^\alpha) \cdot (\tilde{\dot{\boldsymbol{\alpha}}} - \boldsymbol{\eta}^{\dot{\alpha}}) - \boldsymbol{\omega} \times \mathbf{f}_p(\tilde{\boldsymbol{\alpha}} - \boldsymbol{\eta}^\alpha) \quad (19)$$

As detailed in Appendix A, the noise terms from Eq. (19) can be separated, so the measurement can be expressed as:

$$\tilde{\mathbf{v}}_s = \mathbf{v}_s + \boldsymbol{\eta}_s^v \quad (20)$$

$$\boldsymbol{\eta}_s^v = -(\mathbf{H}_p(\tilde{\boldsymbol{\alpha}}) \tilde{\dot{\boldsymbol{\alpha}}} + \boldsymbol{\omega}^\wedge \mathbf{J}_p(\tilde{\boldsymbol{\alpha}})) \boldsymbol{\eta}^\alpha - \mathbf{J}_p(\tilde{\boldsymbol{\alpha}}) \boldsymbol{\eta}^{\dot{\alpha}} \quad (21)$$

where $\mathbf{H}_p(\cdot) \in \mathbb{R}^{3 \times 3 \times 3}$ is the Hessian of the forward kinematics function, $\mathbf{f}_p(\boldsymbol{\alpha})$.

Eq. (20) is valid only when the leg s is in contact with the ground. Since foot contacts happen intermittently while the robot walks, multiple legs can be in contact simultaneously. As each velocity measurement from Eq. (20) is associated with a Gaussian noise term $\boldsymbol{\eta}_s^v$, it would be possible to add to the graph one independent velocity measurement per stance leg. This would however unnecessarily increase the graph complexity, as a closed form for fusing the measurements from the stance legs into one can be computed instead [28]. As $\boldsymbol{\eta}_s^v$ is a linear combination of zero-mean Gaussians, it is

also a zero-mean Gaussian with covariance Σ_s . As a result, a combined velocity measurement for all the stance legs can then be computed as a weighted average of the velocity measurements of each stance leg, based on the information matrix $\Omega_s = \Sigma_s^{-1}$.

$$\Sigma_v = \left(\sum_{s \in S} \Omega_s \right)^{-1} \quad (22)$$

$$\tilde{\mathbf{v}} = \Sigma_v \sum_{s \in S} (\Omega_s \tilde{\mathbf{v}}_s) \quad (23)$$

$$\boldsymbol{\eta}^v \sim \mathcal{N}(\mathbf{0}, \Sigma_v) \quad (24)$$

where the compound velocity measurement noise $\boldsymbol{\eta}^v$ is sampled from a zero-mean Gaussian with covariance Σ_v .

We now have a linear velocity measurement¹ $\tilde{\mathbf{v}}$ and its noise $\boldsymbol{\eta}^v$ that can be used for the preintegrated velocity factor:

$$\tilde{\mathbf{v}} = \mathbf{v} + \boldsymbol{\eta}^v \quad (25)$$

3) *Velocity Bias*: On slippery or deformable terrains, the constraint from Eq. (16) will not be true, resulting in incorrect leg velocities, and thus drift in the final odometry estimate. In our experience, this velocity drift is locally constant and is gait- and terrain-dependent (see Section I-A).

For these reasons, we relax Eq. (16) by adding a slowly varying bias term \mathbf{b}^v to Eq. (25).

$$\tilde{\mathbf{v}} = \mathbf{v} + \mathbf{b}^v + \boldsymbol{\eta}^v \quad (26)$$

this term incorporates the characteristic drift caused by leg or terrain compression, slippage, and impacts occurring at the contact point.

4) *Preintegrated Velocity Measurements*: We derive the preintegrated linear velocity and noise only, as the preintegrated rotation measurement $\tilde{\Theta}_{ij}$ and noise $\delta\theta_{ij}$ have the same form as Eqs. (11) and (14):

$$\Delta\tilde{\Theta}_{ij} = \prod_{k=i}^{j-1} \text{Exp}((\tilde{\omega}_k - \mathbf{b}_i^g) \Delta t) \quad (27)$$

$$\delta\theta_{ij} = \sum_{k=i}^{j-1} \tilde{\Theta}_{k,k+1} \mathbf{J}_R^k \mathbf{b}^{\omega} \Delta t \quad (28)$$

The position at time $t_j = t_i + \Delta t$ is:

$$\mathbf{p}(t_j) = \mathbf{p}(t_i) + \int_{t_i}^{t_j} \mathbf{v}(\tau) d\tau \quad (29)$$

Assuming constant velocity between t_i and t_j , we can iteratively calculate the position in discrete time domain form²:

$$\mathbf{p}_j = \mathbf{p}_i + \sum_{k=i}^{j-1} [\mathbf{R}_k(\tilde{\mathbf{v}}_k - \mathbf{b}_i^v - \boldsymbol{\eta}_k^v) \Delta t] \quad (30)$$

From Eq. (30) a relative measurement can be obtained³:

$$\Delta\kappa_{ij} = \mathbf{R}_i^T(\mathbf{p}_j - \mathbf{p}_i) = \sum_{k=i}^{j-1} [\Delta\mathbf{R}_{ik}(\tilde{\mathbf{v}}_k - \mathbf{b}_k^v - \boldsymbol{\eta}_k^v) \Delta t] \quad (31)$$

With the substitution $\Delta\mathbf{R}_{ik} = \Delta\tilde{\Theta}_{ik} \text{Exp}(-\delta\theta_{ik})$ to include the preintegrated rotation measurement (from Eqs. (27)–(28)), and the approximation $\text{Exp}(\phi) \simeq \mathbf{I} + \phi^{\wedge}$, Eq. (31) becomes:

$$\Delta\kappa_{ij} \simeq \sum_{k=i}^{j-1} [\Delta\tilde{\Theta}_{ik}(I - \delta\theta_{ik}^{\wedge})(\tilde{\mathbf{v}}_k - \mathbf{b}_i^v - \boldsymbol{\eta}_k^v) \Delta t] \quad (32)$$

By separating the measurement and noise components of Eq. (32) and ignoring higher order terms, we can define the *preintegrated leg odometry position measurement* $\Delta\tilde{\kappa}_{ij}$ and *noise* $\delta\kappa_{ij}$ as:

$$\Delta\tilde{\kappa}_{ij} \triangleq \sum_{k=i}^{j-1} [\Delta\tilde{\Theta}_{ik}(\tilde{\mathbf{v}}_k - \mathbf{b}_i^v) \Delta t] \quad (33)$$

$$\delta\kappa_{ij} \triangleq \sum_{k=i}^{j-1} [\Delta\tilde{\Theta}_{ik}\boldsymbol{\eta}_k^v \Delta t - \Delta\tilde{\Theta}_{ik}(\tilde{\mathbf{v}}_k - \mathbf{b}_i^v)^{\wedge} \delta\theta_{ik} \Delta t] \quad (34)$$

Note that both quantities still depend on the twist biases $\mathbf{b}^{\omega}, \mathbf{b}^v$. When these change, we would like to avoid the recomputation of Eq. (33). Given a small change $\delta\mathbf{b}$ such that $\mathbf{b} = \bar{\mathbf{b}} + \delta\mathbf{b}$, we use a first order approximation to find the new measurement:

$$\Delta\tilde{\kappa}_{ij}(\mathbf{b}^{\omega}, \mathbf{b}^v) \simeq \Delta\tilde{\kappa}_{ij}(\bar{\mathbf{b}}^{\omega}, \bar{\mathbf{b}}^v) + \frac{\partial\Delta\tilde{\kappa}_{ij}}{\partial\mathbf{b}^g} \delta\mathbf{b}^{\omega} + \frac{\partial\Delta\tilde{\kappa}_{ij}}{\partial\mathbf{b}^v} \delta\mathbf{b}^v \quad (35)$$

5) *Residuals*: The factor residuals include rotation and translation:

$$\mathbf{r}_{\mathcal{K}_{ij}} = [\mathbf{r}_{\Delta\tilde{\Theta}_{ij}}^T, \mathbf{r}_{\Delta\kappa_{ij}}^T] \quad (36)$$

$$\mathbf{r}_{\Delta\Theta_{ij}} = \text{Log}(\Delta\tilde{\Theta}_{ij}(\mathbf{b}_i^{\omega})) \mathbf{R}_i^T \mathbf{R}_j \quad (37)$$

$$\mathbf{r}_{\Delta\kappa_{ij}} = \mathbf{R}_i^T(\mathbf{p}_j - \mathbf{p}_i) - \Delta\tilde{\kappa}_{ij}(\mathbf{b}_i^{\omega}, \mathbf{b}_i^v) \quad (38)$$

Since Eq. (37) has the same form as Eq. (8), when the same angular velocity measurements are used for both the IMU and leg odometry factor, the following relations hold:

$$\Delta\tilde{\Theta}_{ij} = \Delta\tilde{\mathbf{R}}_{ij} \quad \mathbf{b}^{\omega} = \mathbf{b}^g \quad \delta\theta_{ij} = \delta\phi_{ij} \quad (39)$$

In this case, we can avoid double counting the IMU signal by setting the rotational residual $\mathbf{r}_{\Delta\Theta_{ij}}$ to zero. This was not possible in [12], where an external filter was used.

6) *Covariance*: After simple manipulation of Eq. (34), the covariance of the residual $\mathbf{r}_{\mathcal{K}_{ij}}$ can be computed iteratively:

$$\Sigma_{i,k+1}^{\mathcal{K}} = \mathbf{A}\Sigma_{i,k}^{\mathcal{K}}\mathbf{A}^T + \mathbf{B}\Sigma_{\eta}^{\mathcal{K}}\mathbf{B}^T \quad (40)$$

where the first term evolves from an initial condition of $\Sigma_{i,i}^{\mathcal{K}} = \mathbf{0}$, while the second term $\Sigma_{\eta}^{\mathcal{K}}$ is fixed and taken from sensor specifications. The complete derivation of the multiplicative terms \mathbf{A} and \mathbf{B} are detailed in Appendix B.

C. Bias Residuals

The bias terms are intended to change slowly and are therefore modeled as a Gaussian random walk. The residual term for the cost function is as follows:

$$\begin{aligned} \|\mathbf{r}_{\mathbf{b}_{ij}}\|_{\Sigma_{\mathbf{b}_{ij}}}^2 &\triangleq \|\mathbf{b}_j^g - \mathbf{b}_i^g\|_{\Sigma_{\mathbf{b}_i^g}}^2 + \\ &\quad \|\mathbf{b}_j^a - \mathbf{b}_i^a\|_{\Sigma_{\mathbf{b}_i^a}}^2 + \|\mathbf{b}_j^v - \mathbf{b}_i^v\|_{\Sigma_{\mathbf{b}_i^v}}^2 \end{aligned} \quad (41)$$

¹not to be confused with the IMU preintegrated velocity measurement, $\Delta\tilde{\mathbf{v}}$
²for simplicity, we keep the symbol $\boldsymbol{\eta}^v$ for the noise in the discrete domain

³the variable name change is to avoid confusion with the position measurements and noise from the IMU factor

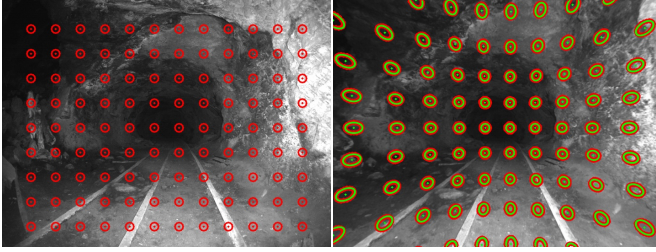


Fig. 5. Example of fisheye covariance warping and fitting. *Left*: Original samples (red points) and 1σ bound of 9 pixels (red circles) in the distorted image. *Right*: the undistorted points from the 1σ bound (red) and their ellipse fit (green) in the undistorted image. Notice that the undistorted covariance becomes larger near the edge of the image where there is greater distortion.

where the covariance matrices are determined by the expected rate of change of these quantities. In particular, $\Sigma_{\mathbf{b}_{ij}^g}$, $\Sigma_{\mathbf{b}_{ij}^s}$ depend on the IMU specifications, while $\Sigma_{\mathbf{b}_{ij}^v}$ depends on the drift rate of the leg odometry bias.

D. Visual Factors

We use two main factors related to visual measurements. The first is a traditional reprojection error given by [21],

$$\mathbf{r}_{\mathbf{x}_i, \mathbf{m}_\ell} = \begin{pmatrix} \pi_u^L(\mathbf{R}_i, \mathbf{p}_i, \mathbf{m}_\ell) - u_{i,\ell}^L \\ \pi_u^R(\mathbf{R}_i, \mathbf{p}_i, \mathbf{m}_\ell) - u_{i,\ell}^R \\ \pi_v(\mathbf{R}_i, \mathbf{p}_i, \mathbf{m}_\ell) - v_{i,\ell} \end{pmatrix} \quad (42)$$

where $(u^L, v), (u^R, v)$ are the pixel locations of the detected landmark. If only a monocular camera is available then the second element of Eq. (42) is not used.

The second factor uses the overlapping fields of view of the lidar and camera sensors (where applicable) to provide depth estimates for visual features, as described in [26].

In addition to the standard camera projective model, in this paper we also introduce support for fisheye cameras with equidistant distortion [29]. To add the landmark to the graph, we first detect and track features in the original, distorted image to avoid costly undistortion. We then undistort the individual feature locations before adding them to the factor graph using Eq. (42).

As shown in Fig. 5, the distortion far from the focal point can be quite large. This means the angular resolution of the camera varies across the image. To correctly model the visual feature uncertainty, $\Sigma_{\mathbf{x}_i, \mathbf{m}_\ell}$, we first select a set of points around the landmark in the distorted image, based on the specified visual feature tracker uncertainty. We then undistort these points and use a least-squares method to fit an ellipse to these points. This gives us an accurate uncertainty matrix in the undistorted image coordinates. Since the distortion is constant, the undistortion map can be precomputed for efficiency.

As demonstrated in [30], a high camera FoV allows for tracking of features for longer periods of time, but for large open areas the loss of pixel density becomes significant for a diagonal FoV of 180° or more. To maximize versatility in underground scenarios, our fisheye configurations have a moderately large diagonal FoV of $150\text{--}165^\circ$ (Table I).

E. Plane and Line Factors

We extract and track geometric primitives, specifically planes and lines, over successive lidar scans. This is similar to how visual features are tracked. Planes are defined using the Hessian norm form [26]:

$$\mathbf{p} = \{(\hat{\mathbf{n}}, d) \in \mathbb{R}^4 \mid \hat{\mathbf{n}} \cdot (x, y, z) + d = 0\} \quad (43)$$

while lines use the minimal parametrization from [31]:

$$\mathbf{l} = \{\langle \mathbf{R}, (a, b) \rangle \in \text{SO}(3) \times \mathbb{R}^2\} \quad (44)$$

In this paper, we extend the plane and line factors from [26] to support local linearization points. This is important in large scale environments, where the transformation of the plane from world to sensor coordinates can cause numerical instability in the optimization (small changes in the angle of the normal can cause very large changes in the position of the plane). This instability increases as the sensor gets further from the origin of the world frame.

Therefore, inspired by [32], we introduce a local linearization frame for planes and lines which we call the anchor frame, \mathbf{A} . This both decreases convergence time [32] and increases numerical stability. \mathbf{A} is arbitrarily defined at the first frame in which the landmark is observed.

When a plane $\tilde{\mathbf{p}}_\ell$ is measured at time t_i , the corresponding residual is the difference between $\tilde{\mathbf{p}}$ and the estimated plane \mathbf{p}_ℓ is transformed into the local reference frame:

$$\mathbf{r}_{\mathbf{x}_i, \mathbf{p}_\ell} = ((\mathbf{T}_{\mathbf{WA}}^{-1} \mathbf{T}_{\mathbf{WB}}) \otimes \mathbf{p}_\ell) \ominus \tilde{\mathbf{p}}_\ell \quad (45)$$

where $\mathbf{T}_{\mathbf{WA}}$ is the pose of the robot at the time where the plane is first detected, $\mathbf{T}_{\mathbf{WB}} = [\mathbf{p}_i, \mathbf{R}_i]$ is the current pose estimate of the robot.

Similarly, the residual between a measured line $\tilde{\mathbf{l}}_i$ and its prediction is defined as follows:

$$\mathbf{r}_{\mathbf{x}_i, \mathbf{l}_\ell} = ((\mathbf{T}_{\mathbf{WA}}^{-1} \mathbf{T}_{\mathbf{WB}}) \boxtimes \mathbf{l}_\ell) \boxminus \tilde{\mathbf{l}}_\ell \quad (46)$$

where \otimes, \boxtimes apply a transformation and \ominus, \boxminus are difference operators to planes and lines, respectively [26].

F. ICP Registration Factor

The lidar feature tracking allows for continuous motion estimation at the full lidar frame rate. Approaches like [33] instead accumulate the features into a local submap for a certain number of frames before integrating them into the factor graph. Local submapping allows for accurate pose estimation refinement, but at a lower frequency. In this work, in addition to the feature tracking, we also integrate fine-grained lidar registration with local submapping. The registration is based on the approach by Ramezani *et al.* [34]. Although ICP typically runs at a lower frequency than the other signals, it is able to take advantage of the high quality motion prior provided by the other modules that run at higher frequency (e.g., IMU) to motion correct scans.

ICP odometry measurements are added into the factor graph as relative pose factors between nonconsecutive keyframes i and m (e.g., nodes 1 and 3 in Fig. 4):

$$\mathbf{r}_{\mathcal{L}_i} = \Phi(\tilde{\mathbf{T}}_i^{-1} \tilde{\mathbf{T}}_m^{-1}, \mathbf{T}_i^{-1} \mathbf{T}_m) \quad (47)$$

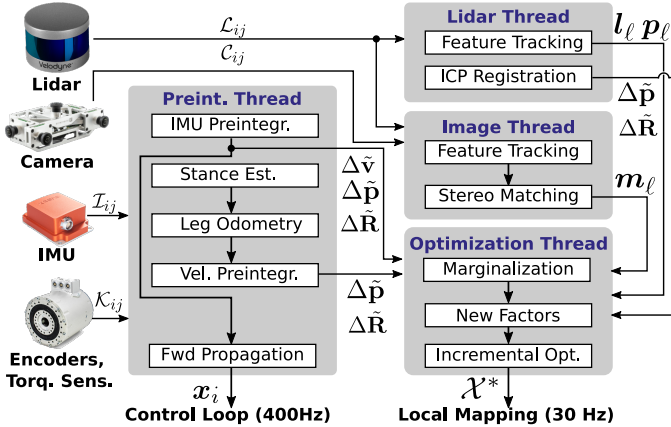


Fig. 6. Block diagram of the VILENS algorithm. Three independent threads (preintegration, camera, and lidar) process the data while a fourth thread performs the optimization on the data already processed by the other threads.

where \mathbf{T} is the estimated pose, $\tilde{\mathbf{T}}$ is the estimate from the ICP module, and Φ is the lifting operator defined in [10]. Note that ICP registration is prone to failure in environments with degenerate geometries, such as long tunnels. For this reason, a robust cost function is used to reject the factor in such degenerate situations.

V. IMPLEMENTATION

The architecture of the VILENS state estimator is shown in Fig. 6. Three parallel threads process the preintegration of IMU and kinematics, camera feature tracking, lidar processing (both feature tracking and ICP registration) and a fourth carries out the subsequent optimization. A forward propagated state from the IMU factor is output from the preintegration thread at IMU frequency (i.e., 400 Hz). This is used to motion correct and synchronize the lidar point clouds (not shown here) and is available for high frequency tasks such as control. When a new keyframe is processed, the preintegrated measurements and tracked landmarks are collected by the optimization thread, while the other threads process the next set of measurements. When the optimization step is complete, the optimal set of states is produced at the keyframe rate for use by local mapping and path planning.

The factor graph is solved using a fixed lag smoothing framework based on the efficient incremental optimization solver iSAM2 [22], implemented as part of the GTSAM library [7]. For these experiments, we use a lag time of 5 s. All visual and lidar factors are added to the graph using the Dynamic Covariance Scaling (DCS) [35] robust cost function to reduce the effect of outliers.

A. Sensor Synchronization

To perform joint optimization across all the sensor modalities, the measurements first need to be synchronized. As in [21], the IMU and kinematic measurements, which have high frequency, are interpolated to match the camera timestamps. To synchronize the lidar measurements with the camera, we instead follow the approach described in [26]. When a new point cloud is received, its points are motion compensated

using the IMU propagated state (from the preintegrated IMU factor) using the closest camera keyframe timestamp as reference, instead of the start or end of the timestamp, as commonly done. In this way, the minimum number of nodes will be added to the graph. The optimization is performed *jointly* between IMU, kinematics, camera and lidar inputs. This also ensures a fixed output frequency, i.e., the camera keyframe rate.

B. Forward Kinematics and Dynamics

The forward kinematics and dynamics are implemented in RobCoGen [36], which is a computationally efficient kinematics and dynamics solver, as demonstrated in this comparison paper [37]. RobCoGen takes the current joint configuration and base state to calculate the position, velocity, and force at each of the feet.

C. Visual and Point Cloud Feature Tracking

We detect visual features using the FAST corner detector, and track them between successive frames using the KLT feature tracker. Outliers are rejected using a RANSAC-based rejection method. For point cloud features, we use the feature tracking approach based on [26] to extract and track geometric primitives (namely planes p_ℓ and lines l_ℓ) over time.

D. Zero Velocity Update Factors

To limit drift and factor graph growth, we continuously query if the robot is stationary by using a voting mechanism. If the majority of sensor modalities detect no motion then we add a zero velocity constraint to the graph.

For example, the IMU and leg odometry threads report zero velocity when position (rotation) is less than 0.1 mm (0.5°) between two keyframes. The image thread reports zero velocity when average feature movement between frames is less than 0.5 pixels. The lidar thread reports zero velocity when the motion induced by planes and lines tracking is less than 0.2 m and 5°, respectively.

VI. EXPERIMENTAL RESULTS

In this section we will describe the platforms and the dataset used in our evaluations (Sections VI-A and VI-B). We will then demonstrate how the tight integration of kinematics into a factor graph framework allows for easy combination of the different sensor modalities (Section VI-C). Finally, we will end with an analysis of specific challenging situations in the dataset, and discuss computational performance (Sections VI-D and VI-E).

A. Experimental Platforms

The platforms used for our experiments are the ANYbotics ANYmal B300 [38] and C100 quadrupeds (Fig. 1). Both robots have 4 identical legs giving a total of 12 active Degrees-of-Freedom (DoF) and are equipped with an IMU and a Velodyne VLP-16 lidar. Each leg has joint encoders, torque sensors. In some of the experiments, the robots were modified from the stock version to compete in the DARPA SubT Challenge as detailed in [39]. This gives a total of three different sensor configurations (see Fig. 1 and Table I).

Sensor	Model	Hz	Specs
Sensors common to ANYmal B300 and C100			
Enc.	ANYdrive	400	<i>Res.</i> : <0.025°
Torque	ANYdrive	400	<i>Res.</i> : <0.1 N m
Lidar	Velodyne VLP-16	10	<i>Res.</i> : 16 px \times 1824 px
ANYmal B300 (experiments: SMR, FSC)			
IMU	Xsens MTi-100	400	<i>Init Bias</i> : 0.2 °/s 5 mg <i>Bias Stab</i> : 10 °/h 15 mg
Gray Stereo Camera	RealSense D435i	30	<i>Res.</i> : 848 px \times 480 px <i>FoV (Diag.)</i> : 100.6°
ANYmal B300 (experiment: SUB)			
IMU	Xsens MTi-100	400	<i>Init Bias</i> : 0.2 °/s 5 mg <i>Bias Stab</i> : 10 °/h 15 mg
RGB Mono Camera	FLIR BFS-U3-16S2C-CS	30	<i>Res.</i> : 1440 px \times 1080 px <i>FoV (Diag.)</i> : 150°
ANYmal C100 (experiments: LSM, SMM)			
IMU	Epson G365	400	<i>Init Bias</i> : 0.1 °/s 3 mg <i>Bias Stab</i> : 1.2 °/h 15 mg
Gray Stereo Camera	SevenSense Alphasense	30	<i>Res.</i> : 720 px \times 540 px <i>FoV (Diag.)</i> : 165.4°

TABLE I
SENSOR SPECIFICATIONS OF THE EXPERIMENTAL PLATFORMS

B. Dataset

To evaluate our proposed algorithm, we have collected datasets in a variety of test environments lasting a total of 2 h and traveling 1.8 km. This includes data from the Urban Circuit of the DARPA Subterranean Challenge (SubT). The dataset is composed of the following experiments:

- **SMR:** Swiss Military Rescue Facility, Wangen, CH. Trotting over concrete & gravel followed by loops on grass with different gaits (ANYmal B300, 106 m, 13 min);
- **FSC:** Fire Service College, Moreton-in-the-Marsh, UK. Three loops of an outdoor industrial environment with standing water, oil residue, gravel and mud (ANYmal B300, 240 m, 34 min);
- **SUB:** DARPA SubT Beta course, Satsop, WA, USA⁴. Autonomous exploration of a dark underground inactive nuclear powerplant (ANYmal B300, 490 m, 60 min);
- **LSM:** A decommissioned limestone mine, Wiltshire, UK. Teleoperated exploration of an unlit mine with several loops (ANYmal C100, 474 m, 20 min);
- **SMM:** Seemühle mine, CH. Autonomous exploration with Cerberus SubT exploration system (ANYmal C100, 522 m, 17 min).

Images from the on-board cameras in each of the experiments are shown in Fig. 7 which illustrate various challenges including slippery ground (affecting kinematics), reflections and darkness (affecting vision), and long corridors (affecting lidar point cloud registration). Different copies of the robots were used in each experiment.

In the SMR and FSC experiments, ground truth was generated by tracking the robot using a Leica TS16 laser tracker

⁴This is the same sequence used in [26], except here we additionally process leg kinematics.



Fig. 7. Onboard camera images showing challenging environments from the experiments. *Top-Left*: wet and oily concrete with reflections and lack of features at the horizon (FSC); *Top-Right*: complete darkness (image manually enhanced in post processing). *Bottom-Left*: low light, overexposure and dust particles (LSM); *Bottom-Right*: long straight corridors and low light (SMM).

and then estimating its orientation using a optimization-based method (as described in [12]). In LSM, SUB, and SMM experiments, an ICP-based method was to align the current lidar scan to an accurate prior map made with survey-grade lidar scanners (as described in [40]).

C. Multi-sensor Fusion Comparison

To evaluate the performance of the system we compute the mean Relative Pose Error (RPE) over distances of 10 m traveled for different module combinations of VILENS (at 15 Hz). We use a letter to indicate the sensor modalities used as follows: lidar features (**L**), visual features (**V**), IMU preintegration (**I**), preintegrated leg kinematics (**K**), ICP registration (**R**).

The set of combinations tested are as follows:

- **VILENS-LVI:** lidar and visual feature tracking with preintegrated IMU but no leg kinematics. This is the same configuration as [26].
- **VILENS-LVK:** lidar and visual feature tracking, with preintegrated IMU and including leg kinematics.
- **VILENS-IR:** only ICP registration and preintegrated IMU. As a fair comparison, we use the IMU to undistort point clouds. In this configuration, the output is limited by the frequency of ICP and thus can only run at 2 Hz.
- **VILENS:** lidar and visual feature tracking, preintegrated IMU, leg kinematics, and ICP registration. This is the full algorithm proposed in this paper. (Where no letters are appended to the word VILENS we mean this version.)

Note that the same settings have been used for all configurations, with just different modules activated for each experiment.

For comparison we also tested CompSLAM [6] which is a loosely coupled filter which combines lidar-inertial odometry (LOAM [41]), visual-inertial odometry (ROVIO [42]), and kinematic-inertial odometry (TSIF [11]). It uses heuristics to

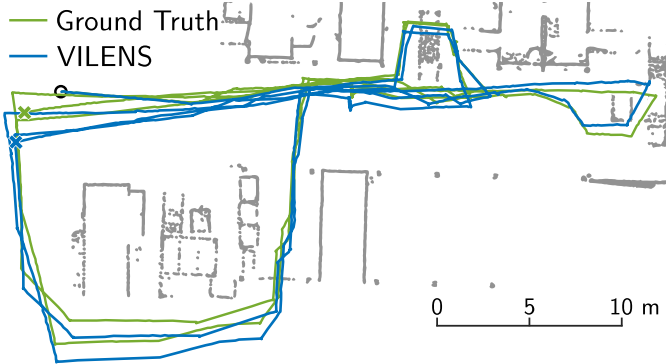


Fig. 8. Aerial view of the estimated and ground truth trajectories on the FSC experiment (240 m traveled). The start of the trajectory is marked with a circle. Ending location is marked with a cross. Note that since VILENS is an odometry system, no loop closures have been performed.

10 m Relative Pose Error (RPE)					
Data	Translation $\mu(\sigma)[\text{m}]$				
	C-S* [6]	V-VLI	V-VLIK	V-IR [†]	VILENS
SMR	0.28 (0.14)	0.14 (0.12)	0.15 (0.12)	0.24 (0.15)	0.12 (0.11)
FSC	0.16 (0.08)	0.20 (0.09)	0.24 (0.17)	0.15 (0.09)	0.15 (0.07)
SUB	0.20 (0.14)	0.11 (0.07)	0.11 (0.08)	0.10 (0.08)	0.05 (0.03)
LSM	0.27 (0.15)	0.34 (0.30)	0.29 (0.33)	0.10 (0.08)	0.04 (0.04)
SMM	0.36 (0.14)	0.74 (0.99)	0.74 (0.90)	0.27 (0.22)	0.12 (0.08)
Data	Rotation $\mu(\sigma)[\text{°}]$				
	C-S* [6]	V-VLI	V-VLIK	V-IR [†]	VILENS
SMR	3.14 (1.83)	1.18 (0.97)	1.38 (1.05)	1.69 (0.93)	1.30 (1.07)
FSC	2.36 (1.07)	1.30 (0.90)	1.17 (0.94)	2.03 (0.86)	1.14 (0.78)
SUB	0.99 (0.62)	0.75 (0.40)	0.74 (0.43)	1.88 (1.13)	0.56 (0.34)
LSM	1.80 (0.94)	2.32 (1.73)	1.92 (1.51)	1.44 (0.71)	0.59 (0.39)
SMM	1.42 (0.73)	4.73 (6.60)	4.38 (5.26)	2.73 (1.73)	1.19 (0.61)

TABLE II

EXPERIMENTAL RESULTS. “C-S*” = COMPSLAM, “V-” = VILENS-, *OUTPUT AT 5 Hz, [†]OUTPUT AT 2 Hz

switch between modalities. LOAM is its primary modality and has a frequency of 5 Hz. CompSLAM was also developed and tested on the ANYmal robots during the DARPA SubT Challenge [39].

Figs. 8 and 9 illustrate the high level performance of VILENS. It can be seen that the estimated trajectory closely matches the ground truth, showing the accuracy of this approach. Note that VILENS is an odometry system — no loop closures are performed in this system. However VILENS can be integrated with an external SLAM system such as [34].

Quantitative results are summarized in Table II. Across the entire dataset, the best performing algorithm was the complete VILENS system, with an overall mean RPE error of just 0.96 % in translation and 0.0956 deg / m in rotation.

Compared to the ICP and IMU only (VILENS-IR) solution VILENS provides higher frequency and higher accuracy estimation, as well as robustness against degenerate scenarios for lidar, including long tunnels. The improvement in performance is due to the incorporation of different sensor modalities at higher frequency. This created a smoother state estimate which improved lidar motion correction, provided a better prior for ICP, and allowed for inaccurate ICP estimates to be rejected using robust cost functions.

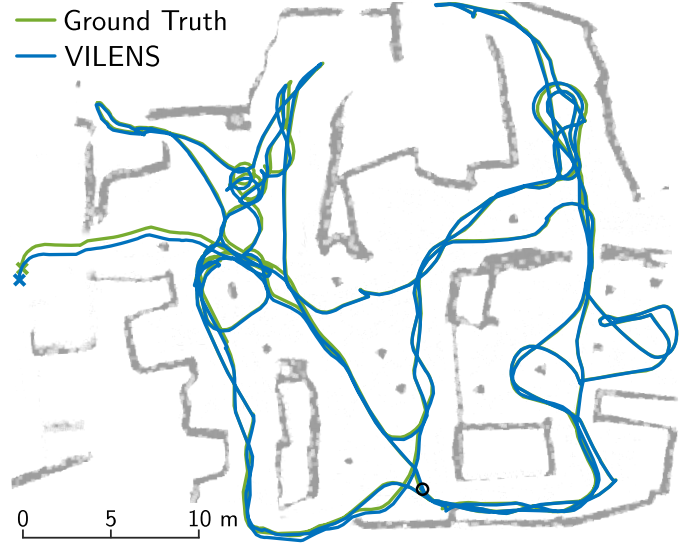


Fig. 9. Top-down view of the trajectory estimate by VILENS (blue) and the ground truth (green) on the 474 m LSM experiment. The start of the trajectory is indicated by a black circle, while the end is indicated with a cross. Note that since VILENS is an odometry system, no loop closures have been performed.

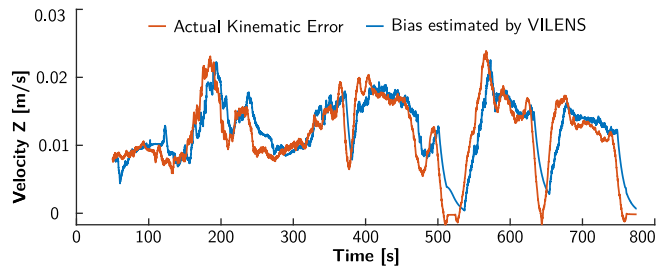


Fig. 10. Comparison between the actual velocity error from the kinematic odometry in the z -axis (inferred using a Leica tracker) and the bias estimated by VILENS during the SMR experiment. Using exteroceptive sensing, VILENS is able to accurately and stably track this effect by modeling the bias term \mathbf{b}^v .

Additionally, VILENS outperforms the loosely coupled approach, CompSLAM, by an average of 62 % in translation and 51 % in rotation.

Accurate, high frequency state estimation is also a requirement for terrain mapping, as discussed in Section VI-E.

D. Discussion

1) *Evolution of Velocity Bias:* In Fig. 10 we compare the actual and the estimated kinematics velocity error in the z -axis. The orange line indicates the error between the true robot velocity and the one perceived by the leg odometry, while the blue line shows the VILENS estimate of the same error, which is modeled as a velocity bias term of the leg odometry factor, \mathbf{b}^v . The sequence analyzed is the same as the one shown in Fig. 2. The high degree of correlation between the two signals demonstrates the effectiveness of leg odometry velocity bias estimation.

2) *Performance in Underconstrained Environments:* In contrast to other recent loosely-coupled approaches to multi-sensor state estimation [6], [43], VILENS naturally handles

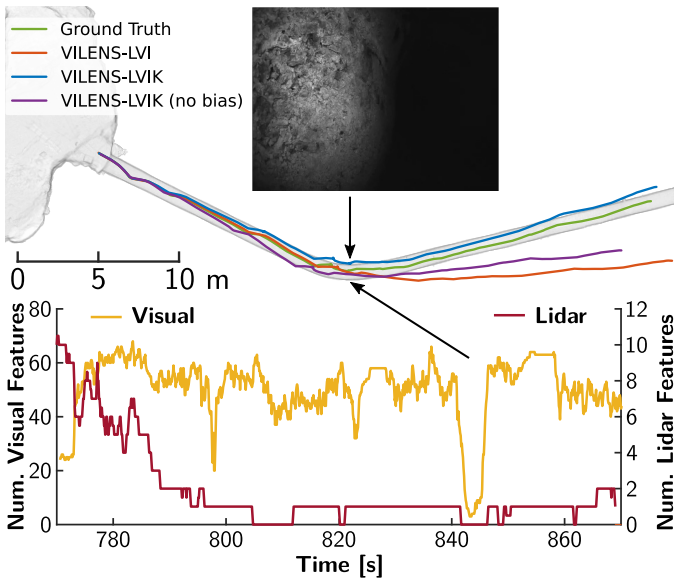


Fig. 11. *Top*: Comparison between the trajectory estimates for different VILENS configurations and ground truth (in green) for the tunnel sequence of the SMM experiment. The lack of visual features causes a large rotation error when not using leg odometry (orange line). Adding leg odometry improves the estimate but still accumulates drift (purple line). With the online velocity bias estimation, the drift is reduced even further (blue line). *Bottom*: number of lidar (in orange) and visual (in blue) features tracked over time.

degenerate scenarios without requiring hard switches which are typically hand engineered.

An example is shown in Fig. 11, where the ANYmal robot walks very close to a wall in a long, straight tunnel. At time 843 s, the robot turns towards the straight part of the tunnel. Due to the degenerate geometry, the number of lidar features gradually drops as the robot goes deeper into the tunnel (maroon line, bottom plot). While the lidar feature tracking can still provide partial constraints to the system, ICP fails. At the same time, the scene changes abruptly causing a period of underexposure (picture at the top), with a dramatic drop in the number of visual features (yellow line, bottom plot). Because of this, the VILENS-LVI configuration (i.e., VILENS without leg odometry and ICP, as in [26]) accumulates a large angular error (orange line). Instead, the addition of leg odometry factor improves the estimate (VILENS-LVIK, blue). To show the benefit of velocity bias estimation, we also show the same VILENS-LVIK configuration but without online bias estimation. Because the terrain is loose, the drift is accumulated faster (purple line).

3) *Leg Odometry in Visually Degraded Scenarios*: Fig. 12 shows a situation from FSC experiment where the robot traverses a large puddle. VILENS-VI tracks the features on the standing water, causing drift in the lateral direction. Instead, VILENS-VIK maintains a better pose estimate by relying on leg odometry with the bias estimation.

E. Terrain Reconstruction Assessment

Constructing an accurate local terrain map around the robot is crucial for perceptive locomotion and path planning. Locomotion controllers plan footstep placements on these maps such as [44].

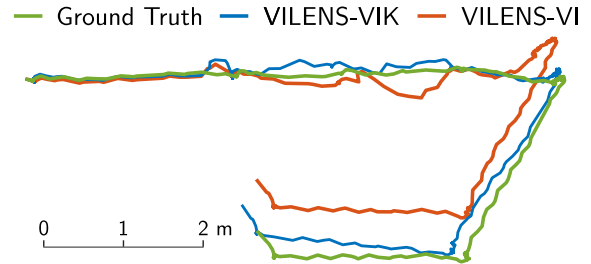


Fig. 12. Top-down comparison of VILENS-VIK and VILENS-VI trajectories aligned with ground truth while crossing the puddle shown in Fig. 7 Top-Left.

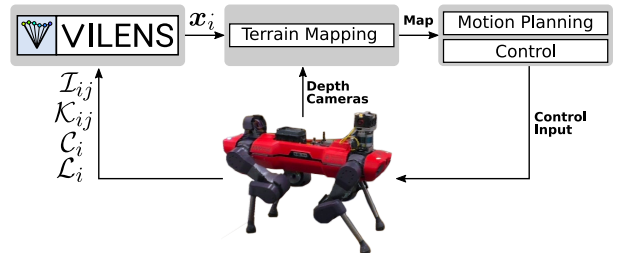


Fig. 13. *Terrain Mapping Pipeline*: The VILENS state estimator produces a high frequency (400 Hz), low drift state estimate, x , for the terrain mapping module [45]. This local terrain map can then be used by other modules, such as perceptive motion planning and control [13], or local path planning for obstacle avoidance [14].

The current approach for the ANYmal robot is to use the kinematic-inertial estimator, TSIF [11], to feed the local elevation mapping system [45]. TSIF can suffer from significant drift, which creates “phantom obstacles” in the terrain map. The effect of this is that the robot exhibits undesirable behavior such as poorly placed foot landings or planning suboptimal paths. In the worst case, the robot may fall and get irreversibly damaged or become stuck because the local path planner is unable to find a feasible solution.

Fig. 13 shows the pipeline used for the terrain mapping with VILENS. The inputs to the terrain mapping module [45] are the VILENS state estimate, and the point clouds from several downward-facing depth cameras on the robot’s body. These cameras are not the same as the ones used for state estimation and are not triggered at the same time. Therefore, accurate terrain mapping depends on a smooth, accurate, and high frequency state estimate to avoid interpolation errors.

From our experience, terrain mapping frequencies of ≥ 15 Hz are required for dynamic locomotion over rough terrain. This means that registration-based algorithms with a low frequency output (such as ICP or LOAM) are not suitable for this purpose.

1) *Terrain Map Integration 1: Local Path Planning*: In the first experiment, we evaluate the quality of online local terrain mapping for local path planning. During the LSM experiment the terrain map was successfully used in the loop by local path planning algorithm, GBPlanner [14], for over 30 min without failure. Fig. 14-Left shows an example of the accuracy of the terrain map compared to the ground truth.

2) *Terrain Map Integration 2: Perceptive Control*: In the second experiment, we demonstrate terrain mapping for perceptive control using RLOC [13]. Fig. 14-Right shows the

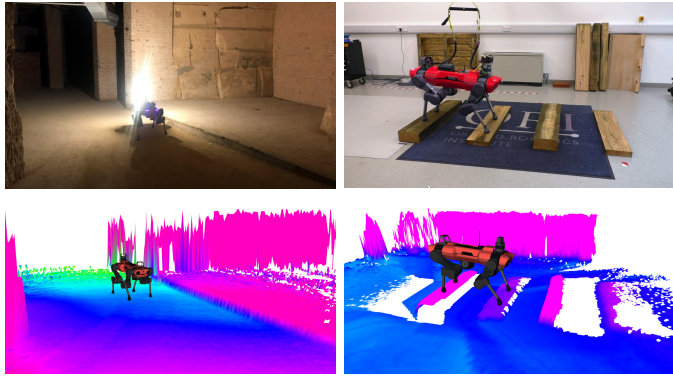


Fig. 14. *Left:* The accurate terrain map generated with the VILENS state estimate can be fed into the local path planner [14] for autonomous exploration. The ledge near the robot is clearly defined in the elevation map, allowing the local planner to create routes on this obstacle. *Right:* The ANYmal robot walking over obstacles using the RLOC perceptive controller [13]. The accurate terrain map produced by using the VILENS estimate enabled successful execution of the trajectory.

Module	Timing $\mu(\sigma)$ [ms]	Freq. [Hz]
IMU	0.05 (0.12)	400
Leg kinematics	0.07 (0.30)	400
Visual features with lidar depth	9.48 (7.69)	10
Lidar point cloud features	19.72 (6.24)	10
Lidar ICP	149.75 (59.23)	2
Optimization	8.65 (3.25)	10

TABLE III
ANALYSIS OF TIMING FOR DIFFERENT PARTS OF VILENS

accuracy of the terrain map, allowing the controller to plan and execute precise steps on the terrain. By reducing the amount drift in the state estimate, the quality of terrain map greatly improves, allowing for more accurate motion planning.

3) *Timing Analysis:* An important consideration in multi-sensor fusion algorithm is computation time, which generally increases with the number of input sensors.

Table III shows a summary of the computation time for the components of VILENS. A key benefit of using this type of factor-graph based approach is that the lightweight visual and point cloud features allow for accurate, low latency state estimation at relatively low computational expense. This also allows more expensive modalities, such as ICP, to run at lower frequency. This saves computation and preserves the benefits of low-drift ICP state estimation.

Table IV highlights the three different types of outputs from the VILENS system, with differing levels of latency and accuracy for different purposes. Fig. 15 shows how the high frequency forward propagated estimate closely matches Vicon ground truth. This is important in some applications to capture the high frequency behavior of the robot between optimizations.

VII. CONCLUSION

This paper presented VILENS, a multi-sensor fusion algorithm which can seamlessly fuse inertial, legged, lidar, and visual sensing within the same factor graph. The tight fusion

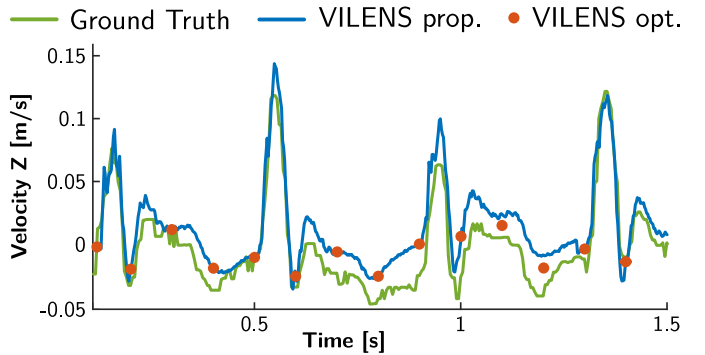


Fig. 15. Comparison between the optimized (10 Hz, orange dots) and IMU forward propagated (400 Hz, blue line) velocity estimates against the ground truth from motion capture (green line). The good tracking of the ground truth shows that IMU forward propagation provides an accurate, high frequency, and low latency prediction of the state between optimizations.

Output type	Mean latency [ms]	Freq. [Hz]
IMU forward-propagated	2.3	400
Factor graph Optimized	95.2	10
ICP optimized	395.2	2

TABLE IV
FREQUENCY AND LATENCY OF OUTPUTS. LATENCY IS COMPARED TO THE LOWEST LATENCY INPUT SIGNAL (IMU)

of all these sensor modalities allows the algorithm to overcome the challenging operational conditions of autonomous navigation in underground environments as well as large open areas. In these conditions, individual sensor modalities such as visual-inertial or lidar-inertial odometry would fail.

A particular contribution of the paper was the integration of the leg kinematic measurements as a dedicated residual for the factor graph, rather than relying on an external filter. This enables tighter integration and better noise modeling. The leg odometry drift, typically occurring due to leg compression at the impact, was modeled as a bias term of the velocity measurement and was proven to be effective in challenging episodes where both the lidar and camera sensors are deprived. In these situations, our system falls back to fusing IMU and leg odometry with no hard switching required.

We demonstrated the robustness of our method in field experiments with several quadruped platforms in challenging scenarios including slippery and deformable terrain, water reflections, complete darkness, and degenerate geometries, such as long corridors lasting longer than two hours.

The high frequency as well as the smoothness of the output was further demonstrated by running the algorithm online and onboard the robot to enable local elevation mapping, which was used by a perceptive controller [13] and a local path planner [14] to cross an obstacle course and to autonomously explore a mine, respectively.

APPENDIX PREINTEGRATED LEG ODOMETRY FACTOR

In this appendix we provide a derivation of the measurements and covariance for the preintegrated leg odometry factor described in Section IV-B. Without loss of generality, we will

focus on cases when only one leg is in contact with the ground. As explained in Section IV-B2, when there are multiple stance legs, the compound measurement and noise can be computed independently from each stance leg and the fused together via a weighted average.

A. Velocity Measurement and Noise

When a leg is in rigid, nonslipping contact with the ground, the robot's linear velocity can be computed from the position and velocity of the feet:

$$\mathbf{v} = -\mathbf{J}_p(\boldsymbol{\alpha})\dot{\boldsymbol{\alpha}} - \boldsymbol{\omega} \times \mathbf{f}_p(\boldsymbol{\alpha}) \quad (48)$$

where $\mathbf{f}_p(\cdot)$ is the forward kinematics function and $\mathbf{J}_p(\cdot)$ its Jacobian. To compute a velocity measurement for the factor graph, we need to linearly separate the noise from the rest of Eq. (48). Remembering from Eqs. (17)–(18) that the joint states are corrupted by zero-mean Gaussian noise, such that $\boldsymbol{\alpha} = \tilde{\boldsymbol{\alpha}} - \boldsymbol{\eta}^\alpha$, $\dot{\boldsymbol{\alpha}} = \tilde{\dot{\boldsymbol{\alpha}}} - \boldsymbol{\eta}^{\dot{\alpha}}$, we first start by separating the noise from the differential kinematics term:

$$\begin{aligned} \mathbf{J}_p(\boldsymbol{\alpha})\dot{\boldsymbol{\alpha}} &= \mathbf{J}_p(\tilde{\boldsymbol{\alpha}} - \boldsymbol{\eta}^\alpha)(\tilde{\dot{\boldsymbol{\alpha}}} - \boldsymbol{\eta}^{\dot{\alpha}}) \\ &= \mathbf{J}_p(\tilde{\boldsymbol{\alpha}} - \boldsymbol{\eta}^\alpha)\tilde{\dot{\boldsymbol{\alpha}}} - \mathbf{J}_p(\tilde{\boldsymbol{\alpha}} - \boldsymbol{\eta}^\alpha)\boldsymbol{\eta}^{\dot{\alpha}} \\ &\simeq \mathbf{J}_p(\tilde{\boldsymbol{\alpha}})\tilde{\dot{\boldsymbol{\alpha}}} - \frac{\partial}{\partial \tilde{\boldsymbol{\alpha}}}(\mathbf{J}_p(\tilde{\boldsymbol{\alpha}})\tilde{\dot{\boldsymbol{\alpha}}})\boldsymbol{\eta}^\alpha - \mathbf{J}_p(\tilde{\boldsymbol{\alpha}})\boldsymbol{\eta}^{\dot{\alpha}} \end{aligned} \quad (49)$$

where we applied the Taylor expansion of the product $\mathbf{J}_p(\boldsymbol{\alpha})\dot{\boldsymbol{\alpha}}$, ignoring the second order terms. Since $\boldsymbol{\alpha}$ and $\dot{\boldsymbol{\alpha}}$ are independent, $\dot{\boldsymbol{\alpha}}$ can be taken out of the derivative in Eq. (49):

$$\frac{\partial}{\partial \tilde{\boldsymbol{\alpha}}}(\mathbf{J}_p(\tilde{\boldsymbol{\alpha}})\tilde{\dot{\boldsymbol{\alpha}}})\boldsymbol{\eta}^\alpha = \frac{\partial}{\partial \tilde{\boldsymbol{\alpha}}}(\mathbf{J}_p(\tilde{\boldsymbol{\alpha}}))\tilde{\dot{\boldsymbol{\alpha}}}\boldsymbol{\eta}^\alpha = \mathbf{H}_p(\tilde{\boldsymbol{\alpha}})\tilde{\dot{\boldsymbol{\alpha}}}\boldsymbol{\eta}^\alpha \quad (50)$$

where $\mathbf{H}_p(\cdot) \in \mathbb{R}^{3 \times 3 \times 3}$ is the Hessian of the forward kinematics function $\mathbf{f}_p(\boldsymbol{\alpha})$. Note that, since the forward kinematics is a vector function, the Hessian becomes a tensor of rank 3, so the product with $\mathbf{H}_p(\tilde{\boldsymbol{\alpha}})\tilde{\dot{\boldsymbol{\alpha}}} = \mathbf{H}_p(\tilde{\boldsymbol{\alpha}}) \bar{\times}_2 \tilde{\dot{\boldsymbol{\alpha}}}$ is a 2-mode vector product [46].

Substituting (49)–(50) into (48) leads to:

$$\begin{aligned} \mathbf{v} &= -\mathbf{J}_p(\tilde{\boldsymbol{\alpha}})\tilde{\dot{\boldsymbol{\alpha}}} - \mathbf{H}_p(\tilde{\boldsymbol{\alpha}})\tilde{\dot{\boldsymbol{\alpha}}}\boldsymbol{\eta}^\alpha - \mathbf{J}_p(\tilde{\boldsymbol{\alpha}})\boldsymbol{\eta}^{\dot{\alpha}} \\ &\quad - \boldsymbol{\omega} \times \mathbf{f}_p(\tilde{\boldsymbol{\alpha}} - \boldsymbol{\eta}^\alpha) \end{aligned} \quad (51)$$

It has been demonstrated in [4] that the noise from the last term of Eq. (51) can be separated as follows:

$$\mathbf{f}_p(\tilde{\boldsymbol{\alpha}} - \boldsymbol{\eta}^\alpha) \approx \mathbf{f}_p(\tilde{\boldsymbol{\alpha}}) - \mathbf{J}_p(\tilde{\boldsymbol{\alpha}})\boldsymbol{\eta}^\alpha \quad (52)$$

From the above relations, Eq. (48) becomes:

$$\begin{aligned} \mathbf{v} &= -(\mathbf{J}_p(\tilde{\boldsymbol{\alpha}})\tilde{\dot{\boldsymbol{\alpha}}} - \mathbf{H}_p(\tilde{\boldsymbol{\alpha}})\tilde{\dot{\boldsymbol{\alpha}}}\boldsymbol{\eta}^\alpha - \mathbf{J}_p(\tilde{\boldsymbol{\alpha}})\boldsymbol{\eta}^{\dot{\alpha}}) \\ &\quad - \boldsymbol{\omega} \times \mathbf{f}_p(\tilde{\boldsymbol{\alpha}} - \boldsymbol{\eta}^\alpha) \\ &= -\mathbf{J}_p(\tilde{\boldsymbol{\alpha}})\tilde{\dot{\boldsymbol{\alpha}}} + \mathbf{H}_p(\tilde{\boldsymbol{\alpha}})\tilde{\dot{\boldsymbol{\alpha}}}\boldsymbol{\eta}^\alpha + \mathbf{J}_p(\tilde{\boldsymbol{\alpha}})\boldsymbol{\eta}^{\dot{\alpha}} \\ &\quad - \boldsymbol{\omega} \times (\mathbf{f}_p(\tilde{\boldsymbol{\alpha}}) - \mathbf{J}_p(\tilde{\boldsymbol{\alpha}})\boldsymbol{\eta}^\alpha) \\ &= -\mathbf{J}_p(\tilde{\boldsymbol{\alpha}})\tilde{\dot{\boldsymbol{\alpha}}} + \mathbf{H}_p(\tilde{\boldsymbol{\alpha}})\tilde{\dot{\boldsymbol{\alpha}}}\boldsymbol{\eta}^\alpha + \mathbf{J}_p(\tilde{\boldsymbol{\alpha}})\boldsymbol{\eta}^{\dot{\alpha}} \\ &\quad - \boldsymbol{\omega} \times \mathbf{f}_p(\tilde{\boldsymbol{\alpha}}) + \boldsymbol{\omega} \times \mathbf{J}_p(\tilde{\boldsymbol{\alpha}})\boldsymbol{\eta}^\alpha \\ &= \underbrace{-\mathbf{J}_p(\tilde{\boldsymbol{\alpha}})\tilde{\dot{\boldsymbol{\alpha}}} - \boldsymbol{\omega} \times \mathbf{f}_p(\tilde{\boldsymbol{\alpha}})}_{\tilde{\mathbf{v}}} - \underbrace{(\mathbf{H}_p(\tilde{\boldsymbol{\alpha}})\tilde{\dot{\boldsymbol{\alpha}}} + \boldsymbol{\omega} \times \mathbf{J}_p(\tilde{\boldsymbol{\alpha}}))\boldsymbol{\eta}^\alpha - \mathbf{J}_p(\tilde{\boldsymbol{\alpha}})\boldsymbol{\eta}^{\dot{\alpha}}}_{\boldsymbol{\eta}^v} \\ &\triangleq \tilde{\mathbf{v}} - \boldsymbol{\eta}^v \end{aligned} \quad (53)$$

Eq. (53) still depends on the rotational velocity, which is measured by the IMU and is affected by measurement noise and bias. If we replace the angular velocity with the measured values, we have:

$$\begin{aligned} \mathbf{v} &= -\mathbf{J}_p(\tilde{\boldsymbol{\alpha}})\tilde{\dot{\boldsymbol{\alpha}}} - (\tilde{\boldsymbol{\omega}} - \mathbf{b}^\omega - \boldsymbol{\eta}^\omega) \times \mathbf{f}_p(\tilde{\boldsymbol{\alpha}}) + \\ &(\mathbf{H}_p(\tilde{\boldsymbol{\alpha}})\tilde{\dot{\boldsymbol{\alpha}}} + (\tilde{\boldsymbol{\omega}} - \mathbf{b}^\omega - \boldsymbol{\eta}^\omega) \times \mathbf{J}_p(\tilde{\boldsymbol{\alpha}}))\boldsymbol{\eta}^\alpha + \mathbf{J}_p(\tilde{\boldsymbol{\alpha}})\boldsymbol{\eta}^v \end{aligned} \quad (54)$$

By applying the inversion rule for the cross product and the distributive property we have:

$$\begin{aligned} \mathbf{v} &= -\mathbf{J}_p(\tilde{\boldsymbol{\alpha}})\tilde{\dot{\boldsymbol{\alpha}}} + \mathbf{f}_p(\tilde{\boldsymbol{\alpha}}) \times \tilde{\boldsymbol{\omega}} - \mathbf{f}_p(\tilde{\boldsymbol{\alpha}}) \times \mathbf{b}^\omega - \mathbf{f}_p(\tilde{\boldsymbol{\alpha}}) \times \boldsymbol{\eta}^\omega + \\ &(\mathbf{H}_p(\tilde{\boldsymbol{\alpha}})\tilde{\dot{\boldsymbol{\alpha}}} - \mathbf{J}_p(\tilde{\boldsymbol{\alpha}}) \times \tilde{\boldsymbol{\omega}} + \mathbf{J}_p(\tilde{\boldsymbol{\alpha}}) \times \mathbf{b}^\omega + \mathbf{J}_p(\tilde{\boldsymbol{\alpha}}) \times \boldsymbol{\eta}^\omega)\boldsymbol{\eta}^\alpha + \\ &\mathbf{J}_p(\tilde{\boldsymbol{\alpha}})\boldsymbol{\eta}^v \end{aligned} \quad (55)$$

After rearrangement and removal of the second order terms, the noise can be again separated as follows:

$$\begin{aligned} \mathbf{v} &\simeq \underbrace{-\mathbf{J}_p(\tilde{\boldsymbol{\alpha}})\tilde{\dot{\boldsymbol{\alpha}}} - \tilde{\boldsymbol{\omega}} \times \mathbf{f}_p(\tilde{\boldsymbol{\alpha}}) + \mathbf{b}^\omega \times \mathbf{f}_p(\tilde{\boldsymbol{\alpha}})}_{\tilde{\mathbf{v}}} - \\ &\underbrace{(-(\mathbf{H}_p(\tilde{\boldsymbol{\alpha}})\tilde{\dot{\boldsymbol{\alpha}}} + \tilde{\boldsymbol{\omega}} \times \mathbf{J}_p(\tilde{\boldsymbol{\alpha}}) - \mathbf{b}^\omega \times \mathbf{J}_p(\tilde{\boldsymbol{\alpha}}))\boldsymbol{\eta}^\alpha)}_{\dots} \\ &\underbrace{-\mathbf{J}_p(\tilde{\boldsymbol{\alpha}})\boldsymbol{\eta}^v + \mathbf{f}_p(\tilde{\boldsymbol{\alpha}}) \times \boldsymbol{\eta}^\omega}_{\boldsymbol{\eta}^v} \\ &\simeq \tilde{\mathbf{v}} - \boldsymbol{\eta}^v \end{aligned} \quad (56)$$

B. Iterative Noise Propagation

By substitution of $\boldsymbol{\eta}^v$ from Eq. (56) into Eq. (34), we can express the preintegrated noises $\delta\boldsymbol{\theta}, \delta\boldsymbol{\kappa}$ in iterative form:

$$\begin{bmatrix} \delta\boldsymbol{\theta}_{i,k+1} \\ \delta\boldsymbol{\kappa}_{i,k+1} \end{bmatrix} = \underbrace{\begin{bmatrix} \Delta\tilde{\boldsymbol{\Theta}}_{k,k+1}^\top & \mathbf{0} \\ -\Delta\tilde{\boldsymbol{\Theta}}_{i,k}(\tilde{\mathbf{v}}_k - \mathbf{b}_i^v) \times \Delta t & \mathbf{I} \end{bmatrix}}_{\mathbf{A}} \begin{bmatrix} \delta\boldsymbol{\theta}_{i,k} \\ \delta\boldsymbol{\kappa}_{i,k} \end{bmatrix} + \underbrace{\begin{bmatrix} \mathbf{J}_R \Delta t & \mathbf{0} & \mathbf{0} \\ -\mathbf{f}_p(\tilde{\boldsymbol{\alpha}}_k) \times & \boldsymbol{\chi}_k & \mathbf{J}_p(\tilde{\boldsymbol{\alpha}}_k) \end{bmatrix}}_{\mathbf{B}} \begin{bmatrix} \boldsymbol{\eta}^\omega \\ \boldsymbol{\eta}^\alpha \\ \boldsymbol{\eta}^{\dot{\alpha}} \end{bmatrix} \quad (57)$$

where:

$$\boldsymbol{\chi}_k = \mathbf{H}_p(\tilde{\boldsymbol{\alpha}}_k)\tilde{\dot{\boldsymbol{\alpha}}}_k + \tilde{\boldsymbol{\omega}} \times \mathbf{f}_p(\tilde{\boldsymbol{\alpha}}_k) - (\mathbf{b}^\omega) \times \mathbf{J}_p(\tilde{\boldsymbol{\alpha}}_k) \quad (58)$$

Eq. (57) can be expressed more compactly as:

$$\boldsymbol{\eta}_{i,k+1}^\Delta = \mathbf{A}\boldsymbol{\eta}_{i,k}^\Delta + \mathbf{B}\boldsymbol{\eta}_k \quad (59)$$

where $\boldsymbol{\eta}_k = [\boldsymbol{\eta}^\omega \ \boldsymbol{\eta}^\alpha \ \boldsymbol{\eta}^{\dot{\alpha}}]^\top$.

From the linear expression (59) and given the covariance $\Sigma_{\boldsymbol{\eta}} \in \mathbb{R}^{9 \times 9}$ of the raw gyro and joint states noises $\boldsymbol{\eta}_k$, the covariance for the factor can be computed iteratively:

$$\Sigma_{i,k+1} = \mathbf{A}\Sigma_{i,k}\mathbf{A}^\top + \mathbf{B}\Sigma_{\boldsymbol{\eta}}\mathbf{B}^\top \quad (60)$$

starting from the initial condition $\Sigma_{i,i} = \mathbf{0}$.

ACKNOWLEDGMENT

This research was part funded by the EU H2020 Project THING and the Innovate UK-funded ORCA Robotics Hub (EP/R026173/1). Fallon was supported by a Royal Society University Research Fellowship and Wisth by a Google DeepMind studentship. This research has been conducted as part of the ANYmal research community. Special thanks to the CERBERUS DARPA SubT Team for providing the data from the challenge runs and the hardware support.

REFERENCES

- [1] M. Bloesch, C. Gehring, P. Fankhauser, M. Hutter, M. A. Hoepflinger, and R. Siegwart, "State estimation for legged robots on unstable and slippery terrain," in *IEEE/RSJ International Conference on Intelligent Robots and Systems*, 2013, pp. 6058–6064.
- [2] M. Camurri *et al.*, "Probabilistic contact estimation and impact detection for state estimation of quadruped robots," *IEEE Robotics and Automation Letters*, vol. 2, no. 2, pp. 1023–1030, 2017.
- [3] F. Jenelten, J. Hwangbo, F. Tresoldi, C. D. Bellicoso, and M. Hutter, "Dynamic locomotion on slippery ground," *IEEE Robotics and Automation Letters*, vol. 4, no. 4, pp. 4170–4176, 2019.
- [4] R. Hartley, M. G. Jadidi, L. Gan, J. Huang, J. W. Grizzle, and R. M. Eustice, "Hybrid contact preintegration for visual-inertial-contact state estimation using factor graphs," in *IEEE/RSJ International Conference on Intelligent Robots and Systems*, 2018, pp. 3783–3790.
- [5] M. Camurri, M. Ramezani, S. Nobili, and M. Fallon, "Pronto: A multi-sensor state estimator for legged robots in real-world scenarios," *Frontiers in Robotics and AI*, vol. 7, pp. 1–18, 2020.
- [6] S. Khattak, H. Nguyen, F. Mascarich, T. Dang, and K. Alexis, "Complementary multi-modal sensor fusion for resilient robot pose estimation in subterranean environments," in *International Conference on Unmanned Aircraft Systems*, 2020, pp. 1024–1029.
- [7] F. Dellaert and M. Kaess, "Factor graphs for robot perception," *Foundations and Trends in Robotics*, vol. 6, pp. 1–139, 2017.
- [8] S. Fahmi, G. Fink, and C. Semini, "On state estimation for legged locomotion over soft terrain," *IEEE Sensors Letters*, vol. 5, no. 1, pp. 1–4, 2021.
- [9] T. Koolen *et al.*, "Design of a momentum-based control framework and application to the humanoid robot atlas," *International Journal of Humanoid Robotics*, vol. 13, no. 1, pp. 1–34, 2016.
- [10] C. Forster, L. Carbone, F. Dellaert, and D. Scaramuzza, "On-manifold preintegration for real-time visual–inertial odometry," *IEEE Transactions on Robotics*, vol. 33, no. 1, pp. 1–21, 2017.
- [11] M. Bloesch, M. Burri, H. Sommer, R. Siegwart, and M. Hutter, "The two-state implicit filter recursive estimation for mobile robots," *IEEE Robotics and Automation Letters*, vol. 3, no. 1, pp. 573–580, 2018.
- [12] D. Wisth, M. Camurri, and M. Fallon, "Preintegrated velocity bias estimation to overcome contact nonlinearities in legged robot odometry," in *IEEE International Conference on Robotics and Automation*, 2020, pp. 392–398.
- [13] S. Gangapurwala, M. Geisert, R. Orsolino, M. Fallon, and I. Havoutis, "RLOC: Terrain-aware legged locomotion using reinforcement learning and optimal control," *arXiv*, 2020.
- [14] T. Dang, M. Tranzatto, S. Khattak, F. Mascarich, K. Alexis, and M. Hutter, "Graph-based subterranean exploration path planning using aerial and legged robots," *Journal of Field Robotics*, vol. 37, no. 8, pp. 1363–1388, 2020.
- [15] T. D. Barfoot, *State Estimation for Robotics*. Cambridge University Press, 2017.
- [16] R. Hartley *et al.*, "Legged robot state-estimation through combined forward kinematic and preintegrated contact factors," in *IEEE International Conference on Robotics and Automation*, 2018, pp. 4422–4429.
- [17] C. Forster, M. Pizzoli, and D. Scaramuzza, "SVO: Fast semi-direct monocular visual odometry," in *IEEE International Conference on Robotics and Automation*, 2014, pp. 15–22.
- [18] M. Fourmy, T. Flayols, N. Mansard, and J. Solà, "Contact forces pre-integration for the whole body estimation of legged robots," in *IEEE International Conference on Robotics and Automation*, 2021.
- [19] F. Grimminger *et al.*, "An open torque-controlled modular robot architecture for legged locomotion research," *IEEE Robotics and Automation Letters*, vol. 5, no. 2, pp. 3650–3657, 2020.
- [20] M. Xie, A. Escontrela, and F. Dellaert, "A factor-graph approach for optimization problems with dynamics constraints," *arXiv*, 2020.
- [21] D. Wisth, M. Camurri, and M. Fallon, "Robust legged robot state estimation using factor graph optimization," *IEEE Robotics and Automation Letters*, pp. 4507–4514, 2019.
- [22] M. Kaess, H. Johannsson, R. Roberts, V. Ila, J. J. Leonard, and F. Dellaert, "ISAM2: Incremental smoothing and mapping using the Bayes tree," *The International Journal of Robotics Research*, vol. 31, no. 2, pp. 216–235, 2012.
- [23] J. Hwangbo, C. D. Bellicoso, P. Fankhauser, and M. Hutter, "Probabilistic foot contact estimation by fusing information from dynamics and differential/forward kinematics," in *IEEE/RSJ International Conference on Intelligent Robots and Systems*, 2016, pp. 3872–3878.
- [24] G. Bledt, P. M. Wensing, S. Ingersoll, and S. Kim, "Contact model fusion for event-based locomotion in unstructured terrains," in *IEEE International Conference on Robotics and Automation*, 2018, pp. 4399–4406.
- [25] P. Furgale, "Representing Robot Pose: The good, the bad, and the ugly," 2014. [Online]. Available: <http://paulfurgale.info/news/2014/6/9/representing-robot-pose-the-good-the-bad-and-the-ugly>
- [26] D. Wisth, M. Camurri, S. Das, and M. Fallon, "Unified multi-modal landmark tracking for tightly coupled lidar-visual-inertial odometry," *IEEE Robotics and Automation Letters*, vol. 6, no. 2, pp. 1004–1011, 2021.
- [27] R. Featherstone, *Rigid Body Dynamics Algorithms*. Springer, 2008.
- [28] T. D. Barfoot and P. T. Furgale, "Associating uncertainty with three-dimensional poses for use in estimation problems," *IEEE Transactions on Robotics*, vol. 30, no. 3, pp. 679–693, 2014.
- [29] J. Kannala and S. S. Brandt, "A generic camera model and calibration method for conventional, wide-angle, and fish-eye lenses," *IEEE Transactions on Pattern Analysis and Machine Intelligence*, vol. 28, no. 8, pp. 1335–1340, 2006.
- [30] Z. Zhang, H. Rebecq, C. Forster, and D. Scaramuzza, "Benefit of large field-of-view cameras for visual odometry," in *IEEE International Conference on Robotics and Automation*, 2016, pp. 801–808.
- [31] C. J. Taylor and D. J. Kriegman, "Minimization on the lie group SO(3) and related manifolds," Yale University, Tech. Rep. 9405, 1994.
- [32] M. Kaess, "Simultaneous localization and mapping with infinite planes," in *IEEE International Conference on Robotics and Automation*, 2015, pp. 4605–4611.
- [33] T. Shan, B. Englot, D. Meyers, W. Wang, C. Ratti, and R. Daniela, "LIO-SAM: Tightly-coupled lidar inertial odometry via smoothing and mapping," in *IEEE/RSJ International Conference on Intelligent Robots and Systems*, 2020, pp. 5135–5142.
- [34] M. Ramezani, G. Tinchev, E. Iuganov, and M. Fallon, "Online lidar-slam for legged robots with robust registration and deep-learned loop closure," in *IEEE International Conference on Robotics and Automation*, 2020, pp. 4158–4164.
- [35] K. MacTavish and T. D. Barfoot, "At all Costs: A comparison of robust cost functions for camera correspondence outliers," in *Conference on Computer and Robot Vision*, 2015, pp. 62–69.
- [36] M. Frigerio, J. Buchli, D. G. Caldwell, and C. Semini, "RobCoGen: A code generator for efficient kinematics and dynamics of articulated robots, based on Domain Specific Languages," *Journal of Software Engineering for Robotics*, vol. 7, no. 1, pp. 36–54, 2016.
- [37] S. M. Neuman, T. Koolen, J. Drean, J. E. Miller, and S. Devadas, "Benchmarking and workload analysis of robot dynamics algorithms," in *IEEE/RSJ International Conference on Intelligent Robots and Systems*, 2019, pp. 5235–5242.
- [38] M. Hutter *et al.*, "ANYmal – a highly mobile and dynamic quadrupedal robot," in *IEEE/RSJ International Conference on Intelligent Robots and Systems*, 2016, pp. 38–44.
- [39] M. Tranzatto *et al.*, "CERBERUS: Deployment at the DARPA Subterranean Challenge Urban Circuit," *Field Robotics*, 2021, accepted, to appear.
- [40] M. Ramezani, Y. Wang, M. Camurri, D. Wisth, M. Mattamala, and M. Fallon, "The Newer College Dataset: Handheld lidar, inertial and vision with ground truth," in *IEEE/RSJ International Conference on Intelligent Robots and Systems*, 2020, pp. 4353–4360.
- [41] J. Zhang and S. Singh, "Low-drift and real-time lidar odometry and mapping," *Autonomous Robots*, vol. 41, no. 2, pp. 401–416, 2017.
- [42] M. Bloesch, M. Burri, S. Omari, M. Hutter, and R. Siegwart, "Iterated extended Kalman filter based visual-inertial odometry using direct photometric feedback," *International Journal of Robotics Research*, vol. 36, no. 10, pp. 1053–1072, 2017.

- [43] M. Palieri *et al.*, “LOCUS: A multi-sensor lidar-centric solution for high-precision odometry and 3d mapping in real-time,” *IEEE Robotics and Automation Letters*, vol. 6, no. 2, pp. 421–428, 2021.
- [44] O. Melon, R. Orsolino, D. Surovik, M. Geisert, I. Havoutis, and M. Fallon, “Receding-Horizon Perceptive Trajectory Optimization for Dynamic Legged Locomotion with Learned Initialization,” in *IEEE International Conference on Robotics and Automation*, June 2021.
- [45] P. Fankhauser, M. Bloesch, and M. Hutter, “Probabilistic terrain mapping for mobile robots with uncertain localization,” *IEEE Robotics and Automation Letters*, vol. 3, no. 4, pp. 3019–3026, 2018.
- [46] T. G. Kolda and B. W. Bader, “Tensor decompositions and applications,” *SIAM Review*, vol. 51, no. 3, pp. 455–500, 2009.



Marco Camurri (Member, IEEE) received the B.Eng. and M.Eng. degrees in Computer Engineering from the University of Modena and Reggio Emilia (Modena, Italy) in 2009 and 2012, respectively. He received his PhD degree in Advanced Robotics in 2017 from the Istituto Italiano di Tecnologia (IIT) in Genoa, Italy.

From 2017 to 2020 he was postdoc at IIT (one year) and University of Oxford (two years).

Since 2021, he is Senior Research Associate at the Oxford Robotics Institute, University of Oxford.

His research interests include legged state estimation, mobile robot perception, sensor fusion, mapping, and mobile autonomous navigation.



David Wisth (Student Member, IEEE) received the B.S. degree in electrical engineering in 2012 and the M.Eng. degree in mechatronics engineering in 2014 from the University of Melbourne, Australia. He is currently pursuing the DPhil. degree in engineering science from the University of Oxford, UK.

From 2015 to 2017, he worked as a Project Engineer at Siemens, Australia. His research interests include multi-sensor fusion, factor graphs, and legged robots.

Mr Wisth’s awards and honors include graduating as valedictorian from his M.Eng. degree, and Best Student Paper Award (Finalist) at the IEEE International Conference on Robotics and Automation in 2021.



Maurice Fallon (Member, IEEE) received his B.Eng (electrical engineering) from University College Dublin, Ireland and his PhD (acoustic source tracking) from University of Cambridge, UK.

From 2008–2012 he was a post-doc and research scientist in MIT Marine Robotics Group working on SLAM. Later, he was the perception lead of MIT’s team in the DARPA Robotics Challenge. From 2017 he has been a Royal Society University Research Fellow and Associate Professor at University of Oxford, UK. He leads the Dynamic Robot Systems Group in Oxford Robotics Institute. His research focuses on probabilistic methods for localization, mapping, dynamic motion planning, and multi-sensor fusion.